

J.C. Massey, Z.X. Chen, M. Stöhr, W. Meier, N. Swaminathan, On the blow-off correlation for swirl-stabilised flames with a precessing vortex core, Combust. Flame 239 (2022) 111741.

The original publication is available at www.elsevier.com

<http://dx.doi.org/10.1016/j.combustflame.2021.111741/>

© <2022>. This manuscript version is made available under the CC-BY-NC-ND 4.0 license <http://creativecommons.org/licenses/by-nc-nd/4.0/>

On the blow-off correlation for swirl-stabilised flames with a precessing vortex core

James C. Massey^{a,*}, Zhi X. Chen^{a,**}, Michael Stöhr^b, Wolfgang Meier^b,
Nedunchezian Swaminathan^a

^a*Department of Engineering, University of Cambridge, Trumpington Street,
Cambridge CB2 1PZ, United Kingdom*

^b*German Aerospace Centre (DLR), Institute of Combustion Technology, Pfaffenwaldring 38-40,
70569 Stuttgart, Germany*

Abstract

Large eddy simulations of turbulent swirl-stabilised flames gradually approaching blow-off conditions in a gas turbine model combustor are undertaken. The global equivalence ratio of the flames is reduced by increasing and decreasing the air and fuel flow rates respectively. The filtered reaction rate for partially premixed combustion is modelled using a presumed joint probability density function flamelet model. The average position of the flame is closer to the fuel nozzle when the global equivalence ratio is decreased, contrary to what is expected. Comparisons are made with simultaneous particle image velocimetry, and acetone and OH planar laser induced fluorescence imaging for the corresponding simulated case. It is demonstrated that the mechanisms leading to local extinction are well captured in the simulation and insufficient mixing induced by the precessing vortex core leads to local extinction. Further analysis of the simulations shows that including heat loss effects within the modelling is important for flames near or approaching

*Corresponding author:

**Senior Research Fellow, Robinson College, Cambridge, United Kingdom.
Email address: jcm97@cam.ac.uk (James C. Massey)

blow-off. The non-adiabatic simulation influences the re-stabilisation of the flame after lift-off and shows that the flame leading edge follows the rotation of the PVC. A blow-off correlation based on the Damköhler number is proposed using the PVC rotation frequency and a chemical time scale. Analysis shows that the simulated flames respond to the correlation and including non-adiabatic flamelets is important for flames approaching blow-off.

Keywords:

Large eddy simulation, Local extinction, Partially premixed flames, Precessing vortex core, Swirling flow

1. Introduction

Swirling flows are typically used in gas turbine (GT) combustors to achieve robust flame stabilisation over a wide range of operating conditions [1]. The central or inner recirculation zone (IRZ) established through vortex breakdown mechanisms in reacting flows with swirl contains hot combustion products including radical species. Heat and mass is transported from the combustion products to ignite the fresh reactant mixtures due to the high-intensity turbulence from the vortex region [2]. However, swirling flows in GT combustors are highly turbulent and often feature large fluctuations in fuel–air mixing. This makes flames susceptible to local extinction at lean conditions, which may ultimately lead to complete flame blow-off [3–5].

Swirling flows contain coherent flow structures, such as a precessing vortex core (PVC), which play a prominent role in flame stabilisation [6, 7]. The PVC is a distinctive feature of swirling flows and is a hydrodynamic instability, which manifests as a coherent structure that oscillates on top of the mean base flow. It

exhibits a frequency that is uniform throughout the domain and is equal to the precession frequency [6]. Although it has been observed in some combustors that the PVC is dampened under reacting conditions [8–10], the PVC highly influences flame stabilisation in combustors, which has been observed in the GT model combustor (GTMC) developed by the German Aerospace Centre (DLR) [11–13]. It has been observed that the PVC enhances fuel–air mixing as well as mixing of burnt and unburnt gases [3, 14, 15] and it can induce large scale flame stretch, roll-up and local extinction, which can be severe for flames near the flammability (specifically lean) limits [5]. It is essential to capture these transient phenomena in combustion modelling and simulations to ensure that the overall flame blow-off behaviour can be simulated with confidence.

Large eddy simulation (LES) with a physically consistent, well-tested and robust sub-grid scale (SGS) combustion model is suitable to capture these transient processes. However, computational studies with the LES framework of flame blow-off characteristics for burners where a PVC is observed are scarce. A relatively simple configuration involving a single axial swirler and a bluff body has been developed by Cavaliere et al. [16] to investigate blow-off and simulations of the non-premixed configuration have also been conducted with some success [17, 18]. This case is geometrically simpler compared to the GTMC studied by DLR [12, 13, 19, 20], which contains two radial swirlers with fuel injected between the central and annular swirling air streams. Hence, the fluid mechanical processes in the GTMC are complex and challenging for numerical modelling. However, recent studies [21–24] have demonstrated that these flow features and flame characteristics can be captured well using a carefully designed flamelet based SGS combustion closure. These simulations demonstrated that the

flame stabilisation and lift-off processes are highly influenced by the PVC. Furthermore, it has been demonstrated that including heat loss effects can influence the flame shape [25] and stability [24, 26, 27]. It is expected that the PVC attributes will be affected by heat loss as previously hinted [24]. Nevertheless, the role of the PVC on local extinction leading to flame blow-off in a burner with a realistic geometry is yet to be investigated and the GTMC developed by DLR serves as an ideal case to study this aspect carefully.

The objectives of this investigation are two-fold. The first is to elucidate the role of flow structures and their interactions with the flame as blow-off is approached by analysing LES results and comparing those results with experimental observations made using simultaneous PIV (particle image velocimetry), and acetone- and OH-PLIF (planar laser induced fluorescence) imaging. The second is to explore if a flame blow-off correlation involving the PVC characteristics can be deduced using the insights gathered from the LES results. These objectives are addressed by considering a specific flame condition, referred to as flame C [5, 12, 13], which is suggested to be close to the blow-off limit for the GTMC. The fuel and air flow rates are carefully and systematically changed from the conditions for flame C towards flame blow-off. The effects of heat loss are also investigated by including heat loss within the filtered reaction rate closure model and through boundary conditions of the combustor wall, as previously described by [24].

This paper is organised as follows. A brief description of the LES and combustion modelling methodologies is presented in section 2. The GTMC and laser diagnostics that are used in the previous study [15] are outlined briefly in sections 3.1 and 3.2. The flame conditions investigated in this study along with their

simulation details are described in section 3.3. The results are discussed in section 4 and concluding remarks are drawn in section 5.

2. Large eddy simulation methodology

The filtered conservation equations for mass and momentum are solved, along with the total enthalpy (sum of the sensible and chemical enthalpies) under the low Mach number assumption. A Poisson equation is used to obtain the modified filtered pressure \bar{p} [28]. The Favre-filtered temperature \widetilde{T} is obtained using the filtered enthalpy transport equation and the filtered density $\bar{\rho}$ is obtained using the equation of state. The SGS eddy viscosity ν_T is obtained using the Smagorinsky model [29] and residual scalar fluxes are modelled using gradient hypotheses [28].

The combustion modelling methodology that is used for this study is based on the previous LES studies by Chen et al. [30] and Massey et al. [24]. The approach employs the *mixedness-reactedness* concept [31] and uses a mixture fraction ξ and a reaction progress variable c to prescribe the local thermochemical states in partially premixed flames. The mixture fraction is calculated using the definition proposed by Bilger [32]. Scaled and unscaled progress variable approaches have been tested in the study by Chen et al. [33], where it is observed that the scaled progress variable approach performs better in capturing local extinction and this approach is used here. The scaled progress variable is defined as $c = \psi/\psi^{\text{eq}}$, where $\psi = Y_{\text{CO}} + Y_{\text{CO}_2}$ and the superscript ‘eq’ denotes the equilibrium value for a given mixture fraction. Transport equations for the Favre-filtered mixture fraction $\widetilde{\xi}$ and progress variable \widetilde{c} , and their sub-grid variances, $\sigma_{\xi,\text{sgs}}^2$ and $\sigma_{c,\text{sgs}}^2$ respectively, are used to describe partially premixed combustion. The molecular diffusion terms in the aforementioned transport equations are taken to be the same

for each species, since the Lewis numbers are close to unity for methane–air mixtures. The sub-grid Scalar Dissipation Rate (SDR) terms $\widetilde{\chi}_{\xi,\text{sgs}}$ and $\widetilde{\chi}_{c,\text{sgs}}$ require modelling. The sub-grid SDR for $\widetilde{\xi}$ is modelled using a linear relaxation model $\widetilde{\chi}_{\xi,\text{sgs}} = C_{\xi}(\nu_T/\Delta^2)\sigma_{\xi,\text{sgs}}^2$ [34, 35]. This algebraic expression is suitable for passive scalars, since their gradients are generated through turbulence. The algebraic model developed in the study by Dunstan et al. [36] is used to model $\widetilde{\chi}_{c,\text{sgs}}$, which includes the effects of chemical reactions, thermal expansion and the multi-scale turbulence–combustion interactions [37].

Since partially premixed combustion is considered in this study, the reaction rate closure should include the contributions from premixed and non-premixed combustion modes. Early studies by Bray developed an LES approach for modelling lifted flames, since partially premixed combustion is present at the flame root. An expression for a flame index based on the scalar product of the fuel and oxidiser normal vectors is proposed to quantify the contributions of premixed and non-premixed combustion regimes [38]. It is often convenient to use a reaction progress variable to mark the reaction zones by normalising a scalar variable, which must increase monotonically across the flame. In addition, it is convenient to use a probability density function (PDF) closure in mixture fraction and progress variable space, since the lower and upper limits for both variables are zero and unity respectively, as suggested in the study by Bray et al. [39]. However, the aforementioned study demonstrates that additional scalar dissipation rate terms arise during the normalisation of the progress variable transport equation and these must not be neglected to ensure physical consistency in partially premixed flames. Therefore, the filtered reaction rate source term for partially premixed combustion $\overline{\omega}^*$ should include these additional terms and this is written

as [39]

$$\overline{\dot{\omega}^*} = \underbrace{\frac{\overline{\dot{\omega}_\psi}}{\overline{\psi^{\text{eq}}}}}_{\text{Premixed } \overline{\dot{\omega}_{\text{fp}}}} + \underbrace{\frac{\overline{\rho \chi_\xi \frac{c}{\psi^{\text{eq}}} \frac{d^2 \psi^{\text{eq}}}{d\xi^2}}}{\overline{\psi^{\text{eq}}}}}_{\text{Non-premixed } \overline{\dot{\omega}_{\text{np}}}} + \underbrace{\frac{\overline{2 \rho \chi_{\xi c} \frac{1}{\psi^{\text{eq}}} \frac{d\psi^{\text{eq}}}{d\xi}}}{\overline{\psi^{\text{eq}}}}}_{\text{Cross dissipation term } \overline{\dot{\omega}_{\text{cdr}}}}. \quad (1)$$

The three terms on the right-hand side of Eq. (1) represent the contributions from premixed and non-premixed combustion modes, and their interactions resulting from the cross dissipation rate. These are denoted as $\overline{\dot{\omega}_{\text{fp}}}$, $\overline{\dot{\omega}_{\text{np}}}$ and $\overline{\dot{\omega}_{\text{cdr}}}$ respectively. The cross dissipation term is neglected following previous studies [39, 40].

The first term of Eq. (1) signifies the contribution of the premixed combustion mode, where the unscaled reaction rate is $\dot{\omega}_\psi = \dot{\omega}_{\text{CO}} + \dot{\omega}_{\text{CO}_2}$. This term is modelled as [40]

$$\overline{\dot{\omega}_{\text{fp}}} = \overline{\rho} \int_0^1 \int_0^1 \frac{\dot{\omega}_{\text{fp}}(\eta, \zeta)}{\rho(\eta, \zeta)} \widetilde{P}(\eta, \zeta) d\eta d\zeta, \quad (2)$$

where η and ζ are the sample space variables for the mixture fraction and progress variable respectively. The flamelet reaction rate and density, denoted $\dot{\omega}_{\text{fp}}(\eta, \zeta)$ and $\rho(\eta, \zeta)$ respectively, are obtained from laminar flame calculations using Cantera [41] with the GRI-Mech 3.0 chemical mechanism. The density-weighted joint PDF is approximated using statistically independent beta PDFs as $\widetilde{P}(\eta, \zeta) \approx \widetilde{P}_\beta(\eta; \widetilde{\xi}, \sigma_{\xi, \text{sgs}}^2) \times \widetilde{P}_\beta(\zeta; \widetilde{c}, \sigma_{c, \text{sgs}}^2)$. The premixed combustion source term $\overline{\dot{\omega}_{\text{fp}}}$ can be modified to include non-adiabatic effects at the flamelet level as demonstrated in the study by Massey et al. [24], which applies a heat release damping approach by scaling the source term in the one-dimensional energy equation [42]. The filtered premixed reaction rate source term is modelled as [24]

$$\overline{\dot{\omega}_{\text{fp}}} = \overline{\rho} \int_0^1 \int_0^1 \int_0^1 \frac{\dot{\omega}_{\text{fp}}(\eta, \zeta, \mathcal{H})}{\rho(\eta, \zeta, \mathcal{H})} \widetilde{P}(\eta, \zeta, \mathcal{H}) d\eta d\zeta d\mathcal{H}, \quad (3)$$

where $\widetilde{P}(\eta, \zeta, \mathcal{H}) \approx \widetilde{P}_\beta(\eta; \widetilde{\xi}, \sigma_{\xi, \text{sgs}}^2) \times \widetilde{P}_\beta(\zeta; \widetilde{c}, \sigma_{c, \text{sgs}}^2) \times \delta(\mathcal{H} - \widetilde{h}^*)$ is the joint PDF of

the mixture fraction, progress variable and normalised enthalpy and \mathcal{H} denotes the sample space variable for the normalised enthalpy $h^* = [h - h_{\min}(\xi, c)]/[h_{\text{ad}}(\xi, c) - h_{\min}(\xi, c)]$, where the subscripts ‘min’ and ‘ad’ denote the minimum and adiabatic mixture enthalpies respectively at a given mixture fraction and progress variable. A Dirac delta function is used for h^* . The values of h_{\min} and h_{\max} are tabulated as functions of ξ and c for the normalisation of the filtered enthalpy in the LES. The laminar flame solutions are used for the integration of the PDFs to generate look-up tables containing the filtered quantities. These look-up tables have four dimensions for adiabatic simulations and five dimensions for non-adiabatic simulations; the complete details for generating these look-up tables and their dimensions are outlined by Massey [43].

The non-premixed contribution in Eq. (1) is modelled using [40]

$$\bar{\omega}_{\text{np}} = \bar{\rho} \bar{c} \bar{\chi}_{\xi} \int_0^1 \frac{1}{\psi^{\text{eq}}(\eta)} \frac{d^2 \psi^{\text{eq}}(\eta)}{d\eta^2} \bar{P}(\eta) d\eta. \quad (4)$$

The non-premixed contribution does not come from counterflow diffusion flamelets and is instead a correction term for the premixed source term. This term contains the filtered mixture fraction scalar dissipation rate, which is the sum of the resolved and SGS contributions $\bar{\chi}_{\xi} = \bar{\mathcal{D}}(\nabla \tilde{\xi} \cdot \nabla \tilde{\xi}) + \bar{\chi}_{\xi, \text{sgs}}$. The non-premixed contribution is only significant in the regions where there is a stoichiometric fuel–air mixture, since $d^2 \psi^{\text{eq}}/d\eta^2$ approaches zero for mixtures that are far away from stoichiometric conditions [40]. It has been observed that near-stoichiometric mixtures are located far from the combustion chamber walls in the GTMC, as observed in the experiments [12] and simulations [24]. Thus, this term is taken to be unaffected by heat loss through the combustion chamber walls.

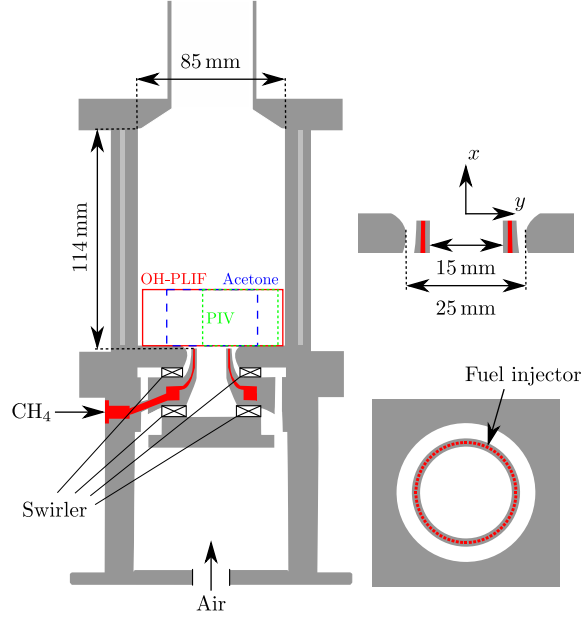


Fig. 1: Schematic of the DLR gas turbine model combustor along with the regions for laser diagnostics [12, 13, 15].

3. Experimental methods and computational procedure

3.1. Gas turbine model combustor

The GTMC developed by DLR is illustrated in Fig. 1 [12, 13]. Dry air at atmospheric pressure and room temperature enters a single plenum and the flow is split through two radial swirlers. The two co-swirling flows enter the combustion chamber through a central nozzle of diameter 15 mm and an annular nozzle with inner and outer diameters of 17 mm and 25 mm respectively, which is contoured to a diameter of 40 mm. Non-swirling methane is fed through a nozzle ring containing 72 channels ($0.5 \times 0.5 \text{ mm}^2$), as shown in Fig. 1. The exit planes of the central air and fuel nozzle ring are 4.5 mm below the exit of the annular divergent air nozzle and the entrance to the combustion chamber. This location corresponds to $x = 0$, as shown in Fig. 1. The combustion chamber has a square cross-section

with an internal area of $85 \times 85 \text{ mm}^2$ and a length of 114 mm. The side walls are formed by 4 quartz plates that are held by 4 posts (diameter 10 mm) in the corners, in order to allow good optical access to the flame. A conical top plate with a central exhaust pipe of diameter 40 mm forms the exit.

3.2. *Measuring techniques*

For assessment of the simulation, the study employs time-resolved, simultaneous measurements of flow field, flame structure and fuel distribution. The main features of the experiment are described below, while further details are provided in the study by Stöhr et al. [15]. The diagnostic set-up consists of a PIV and PLIF system with a repetition rate of 10 kHz. The PLIF systems enables the simultaneous measurement of OH and acetone, which is seeded in small amounts into the methane in order to image the fuel distribution. For the measurements of the flow field using PIV, titanium dioxide (TiO_2) particles with a nominal diameter of $1 \mu\text{m}$ are added to the air flow. The purpose of the combined measuring system is to qualitatively examine the interactions between the flow field, fuel–air mixing processes and the flame. The measurements are obtained in the x – y midplane at $z = 0$, where the PIV and PLIF laser sheets have a thickness of 0.7 mm and 0.4 mm respectively. The PIV measurements are limited to a region bounded by $-4 < y < 36 \text{ mm}$ and $0 < x < 30 \text{ mm}$. The PLIF images are obtained over the same height. The OH-PLIF field width is within $-37 < y < 39 \text{ mm}$ and the acetone-PLIF field width is within $-25 < y < 28 \text{ mm}$. These regions are illustrated in Fig. 1.

3.3. Simulation details

The conditions of the flames analysed in this study are listed in Table 1. The first case, flame C, is investigated using the LES framework described in section 2 and validated against the measurements [23]. The non-adiabatic flamelet formulation is also tested for flame C in the study by Massey et al. [24] and is referred to as flame C-NAD in this study. Measurements are only available for the air and fuel flow rates used for flames C and C-NAD and comparisons with time-averaged statistics are shown in previous studies [23, 24]. The measurements obtained using the PIV and PLIF systems described in section 3.2 are used as further validation for flame C. The air and fuel mass flow rates are $\dot{m}_{\text{air}} = 4.68 \text{ g/s}$ and $\dot{m}_{\text{CH}_4} = 0.15 \text{ g/s}$ respectively giving a global equivalence ratio of $\phi_{\text{glob}} = 0.55$ for flame C [12, 13]. The additional simulations have lower values of ϕ_{glob} , which is achieved by increasing the air mass flow rate or decreasing the fuel mass flow rate. Flames C-F20 and C-F40 represent a decrease in \dot{m}_{CH_4} by 20 % and 40 % respectively, and flame C-A25 represents an increase in \dot{m}_{air} by 25 %. The flow rates are carefully chosen for flames C-A25 and C-F20, in order to decrease the global equivalence ratio to approximately $\phi_{\text{glob}} = 0.45$, and the global equivalence

Case	Flow rates		ϕ_{glob}	Adiabatic flamelets
C [23]	\dot{m}_{air}	\dot{m}_{CH_4}	0.55	Y
C-NAD [24]	\dot{m}_{air}	\dot{m}_{CH_4}	0.55	N
C-F20	\dot{m}_{air}	$0.8 \dot{m}_{\text{CH}_4}$	0.45	Y
C-F40	\dot{m}_{air}	$0.6 \dot{m}_{\text{CH}_4}$	0.35	Y
C-A25	$1.25 \dot{m}_{\text{air}}$	\dot{m}_{CH_4}	0.45	Y
C-A25-NAD	$1.25 \dot{m}_{\text{air}}$	\dot{m}_{CH_4}	0.45	N

Table 1: Mass flow rates and global equivalence ratios for the simulations undertaken.

ratio for flame C-F40 is $\phi_{\text{glob}} = 0.35$. Flame C-A25-NAD is run under the same conditions as flame C-A25, but uses the non-adiabatic flamelet formulation and wall boundary conditions. The bottom plane of the combustion chamber is specified to be at 700 K and the temperature of the side walls increases from 700 K to 1000 K linearly over a height of 40 mm and beyond this height, the temperature is held at 1000 K [24].

The computational grid is the same as used in previous studies [23, 24], which is an unstructured grid with 20 million tetrahedral cells. Previous studies [21, 22] have shown that this numerical grid is adequate for a flame that has a higher Damköhler number and mass flow rates than the cases studied here. The suitability of this grid for the increased flow rates used for this study is also assessed through Pope’s criterion for isothermal flows. The flames listed in Table 1 have global equivalence ratios that are equal or less than in flame C and since the flames in these cases are weaker, the grid resolution is adequate.

The computational model includes an air feed pipe, the plenum, both swirlers and the combustion chamber; this is shown in Fig. 2. A large cylindrical atmospheric far-field downstream of the combustion chamber is included with a coflow air stream to prevent acoustic wave reflection. All 72 fuel injectors are included in the mesh to provide an improved accuracy for the fuel–air mixing field. Five mesh points with a uniform spacing of 0.1 mm are used for the fuel nozzle. There is also refinement along the outer contoured wall of the annular nozzle to ensure that the flow separation is accurately captured. At least two cells adjacent to the wall are within $y^+ < 5$, in order to ensure that the velocity field in those regions is insensitive to the use of a wall model. It is also demonstrated by Massey [43] that the Smagorinsky model produced the best comparisons with the measured velocity

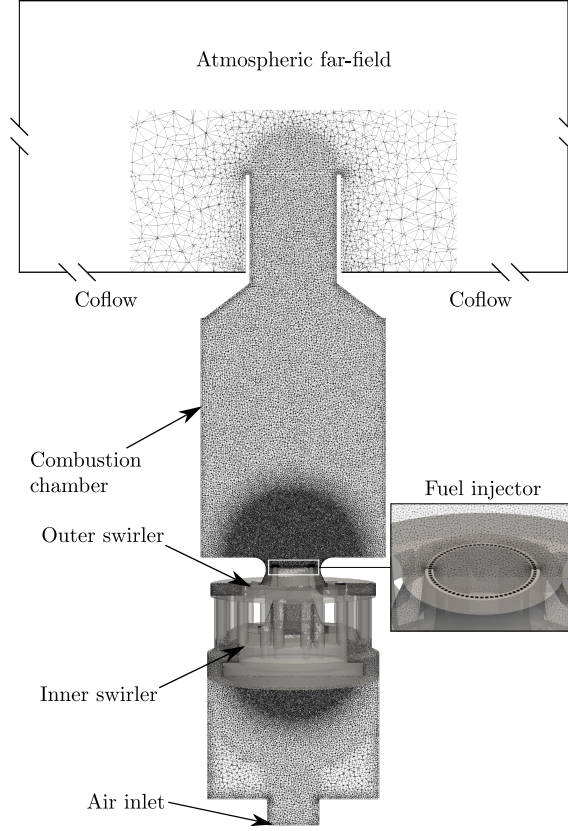


Fig. 2: Computational model of the GTMC.

components for the isothermal flow case by investigating the sensitivity to various sub-grid stress models, which include the k -equation [44] and wall-adapting local eddy (WALE) [45] models. In particular, the flow separation along the contoured wall of the annular divergent nozzle, which affects the jet opening angle and the near-field recirculation zone structure, is captured best by the Smagorinsky model. The studies on flame C [23, 24] also have demonstrated that the velocity fields are well captured with this set-up. The minimum cell sizes around the fuel nozzle, swirlers and shear layers are 0.1, 0.3 and 0.5 mm respectively. The mass flow rates are imposed using the values in Table 1 with top-hat velocity profiles and the

coflow velocity is 0.1 m/s. All walls have no-slip conditions imposed except for the lateral walls of an extended far-field domain beyond the combustion chamber exit, which have slip conditions imposed.

The simulations are undertaken using OpenFOAM 2.3.0 with the PIMPLE algorithm for the pressure–velocity coupling. Second-order central difference schemes with no blending factors are used for the velocity. To ensure numerical stability, an implicit Euler scheme is used for time marching, but with a small time step of $\Delta t = 0.15 \mu\text{s}$. This ensures that the CFL number remains below 0.4 across the whole domain with suitable accuracy for the time derivatives. The simulations are undertaken using 1080 cores on the ARCHER high performance computing service in the United Kingdom.

4. Results

4.1. Averaged flame features

The structure of the IRZ is highly sensitive to the incoming mass flow rate and the global equivalence ratio, since the heat release strongly influences its structure [46]. The IRZ contours are marked by using isolines of the time- and azimuthally-averaged axial velocity $\langle \tilde{U} \rangle = 0$, as shown in Fig. 3. These are shown for the flames with lower global equivalence ratios and compared against flame C and its non-adiabatic counterpart flame C-NAD [24]. Time-averaged contours are not available for flame C-F40, since failed ignition occurred globally. The time-averaged statistics are collected over a 45 ms period. It is observed that the forward stagnation point is located at $x = -5 \text{ mm}$ for all of the cases. However, the size and shape of the IRZ changes significantly in the downstream locations beyond $x \geq 10 \text{ mm}$. In general, it is seen that the IRZ is narrowest for flame C,

since this case has the highest global equivalence ratio and therefore, the strongest heat release. The competing effects of dilatation and turbulence influence the radial pressure forces acting on the IRZ [46], but also the effect of swirling flow and pressure oscillations influence the volume and shape of the IRZ in this configuration [22]. It is shown that including non-adiabatic effects for the SGS reaction rate model causes the recirculation zone width to increase, as observed for flame C-NAD in Fig. 3. The rear stagnation point is located further upstream at $x = 63$ mm for flame C-NAD compared to flame C, where this is located at $x = 68$ mm. The rear stagnation point is located at approximately $x = 68$ mm for flame C-F20, whereas this point is located slightly upstream at $x = 64$ mm for flame C-A25. This is caused by the increase in \dot{m}_{air} , as increasing the flow rate leads to a higher swirl number and leads to a wider recirculation zone [12]. The recirculation zone in the non-adiabatic simulation, flame C-A25-NAD, is almost the same as in flame C-A25 up to $x = 30$ mm. However, the recirculation zone is wider downstream of $x = 30$ mm for flame C-A25-NAD and the rear stagnation point is located at $x = 69$ mm.

The time-averaged filtered mixture fraction contours at $\langle \tilde{\xi} \rangle = 0.04, 0.055$ and 0.08 are shown in Fig. 4 using coloured lines for the same four cases shown in Fig. 3. The top row shows flames C and C-F20 in Figs. 4a and 4b respectively, while the bottom row shows flames C-A25 and C-A25-NAD in Figs. 4c and 4d respectively. It is observed that the isoline of $\langle \tilde{\xi} \rangle = \xi_{\text{st}} = 0.055$ for flame C extends up to $x = 10$ mm. However in the other three cases, this isoline is closer to the fuel nozzle region, which is due to a decreased global equivalence ratio. This is also indicated by the mixture fraction contour $\langle \tilde{\xi} \rangle = 0.04$ spanning a greater area for flame C in Fig. 4a. The stoichiometric mixture fraction contours for

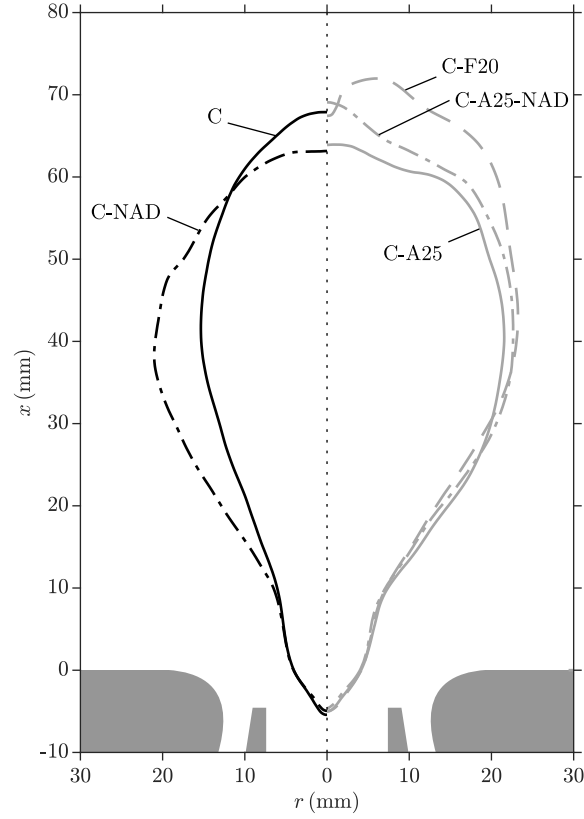


Fig. 3: Isolines of the time-averaged axial velocity contour $\langle \tilde{U} \rangle = 0$ for the simulations listed in Table 1.

the other three cases are similar, suggesting that the near-field mixing region is unaffected by the change in the fuel or air flow rates to achieve a given global equivalence ratio, or by heat loss effects. The $\langle \tilde{\xi} \rangle = 0.04$ contour for flame C-F20 does cover a larger area, suggesting that increasing the air flow rate gives a locally leaner mixture around the flame compared to reducing the fuel flow rate. The black lines in Fig. 4 indicate the averaged flame position using $0.8 \langle \tilde{\omega}^* \rangle_{\max}$. It is shown in Fig. 4 that the flame brush is closer to the fuel nozzle in flames C-F20 and C-A25 than in flame C, since stoichiometric mixtures are closer to the fuel nozzle. The mean lift-off height (based on the flame leading edge on the

$\widetilde{T} = 1500$ K iso-surface above the fuel injectors within $r \leq 10$ mm) over a 300 ms sample for flame C is determined to be 8.32 mm for flame C, whereas this value is marginally further upstream for flames C-A25 and C-F20 at 7.46 mm and 7.89 mm respectively. The use of $\widetilde{T} = 1500$ K to locate the flame brush leading edge is based on the suggestion in previous studies including lifted jet flames [23, 30]. The leading edge in flame C-A25-NAD is further downstream in comparison to flame C-A25 and has a mean lift-off height of 8.99mm. However, the flame base is typically in the same region for all cases, despite the differences in the mass flow rates and inclusion of non-adiabatic effects.

The canonical lifted jet flame has different stabilisation mechanisms, which include premixed flame propagation [47], flame quenching due to high scalar dissipation rates [48], edge flame phenomena [49] and neighbouring large-scale eddies supplying hot products to the edges of the jet [50]. When the fuel jet is diluted with air for a given jet velocity (reducing the global equivalence ratio), the mean flame base is located further downstream [51, 52]. For the configuration studied here, the mean flame lift-off height is similar even when the global equivalence ratio is changed. It is intriguing that for the adiabatic cases where the global equivalence ratio is smaller, the average position of the flame moves further upstream in comparison to flame C. However, the stabilisation mechanisms are different due to the swirling flow field and the presence of the PVC. In addition, flame C-A25-NAD moved downstream compared to flame C-A25, suggesting the important role of including heat loss effects. Therefore, the local mechanisms of flame stabilisation are investigated in the following sections.

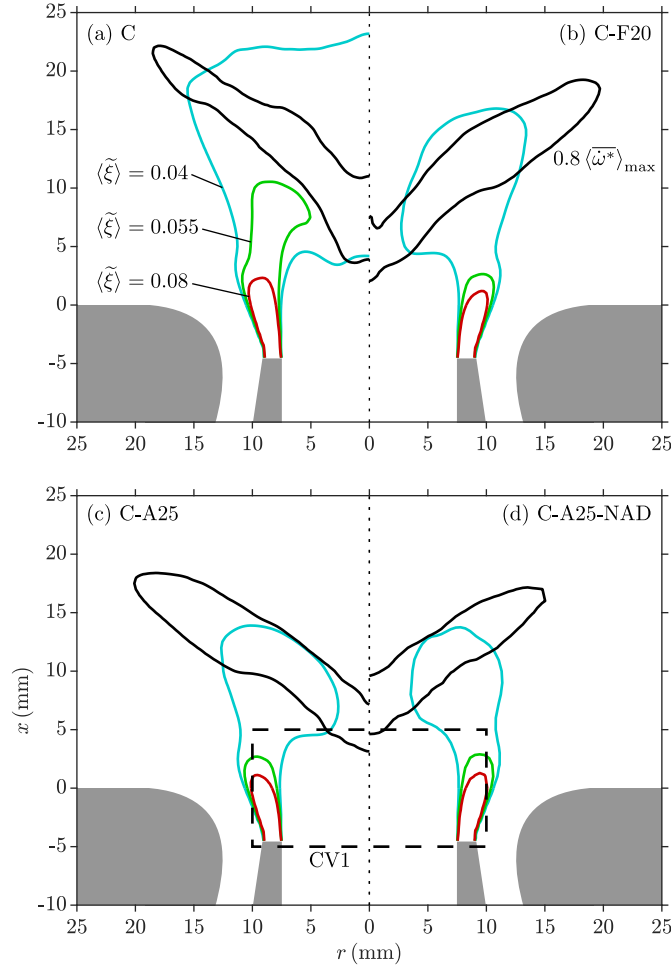


Fig. 4: Isolines of the time-averaged flame position (black lines) and the mixture fraction (coloured lines). The flame position is marked using $0.8 \langle \tilde{\omega}^* \rangle_{\max}$. The control volume CV1 that is marked is used to calculate the volume integrated heat release rate in the nozzle region.

4.2. Comparisons with planar image measurements

As observed in the experimental studies, the flame stabilisation mechanisms are closely coupled to the PVC that rotates periodically at a frequency set by the incoming air flow rate [19]. Its presence enhances fuel–air mixing [15], and can also induce flame roll-up and local extinction [5], which has also been ob-

served numerically for flame C [23]. In addition, pressure fluctuations induced by thermo-acoustic instabilities can cause the PVC to extend axially and retract, as observed in experimental [53] and numerical [22] studies. Frequent disappearance of the flame root is also observed during large pressure fluctuations, and the root of the PVC contracts and expands radially for high and low pressures respectively. The flame root is observed to reform when the pressure fluctuations become smaller, which is also observed in the experimental study by Boxx et al. [54]. Flame C uses the same air mass flow rate as the case with thermo-acoustic instabilities, referred to as flame B, but the lower fuel flow rate used in flame C causes the flame to be close to the lean blow-off limit. Since the pressure fluctuations are small for flame C [55], the stoichiometric mixture fraction remains further away from the PVC and mixing enhancement is weakened. This occasionally leads to local extinction during a later flame roll-up process [5]. If the flame root is not present and flame roll-up does not occur over a critical length of time, which has been estimated to be equal to the time period of one rotation of the PVC, then the flame lifts off (recedes downstream).

As previously mentioned, the flame root and its azimuthal position are highly influenced by the PVC. The PVC frequency f_{pvc} can be obtained through a power spectral analysis of the axial velocity field. The Fast Fourier Transform (FFT) is applied to the axial velocity obtained over a 300 ms period at a point where the PVC is expected to be present; the total duration of the PIV sample is 800 ms with a repetition rate of 5 kHz [5]. This is shown for flame C in the inset of Fig. 5a for a probing point located within the inner shear layer at $x = 13.5$ mm and $y = 9$ mm. The PVC frequency for the LES case is 390 Hz, whereas the frequency obtained using the PIV measurements is 510 Hz. It is observed in the study by Massey et al.

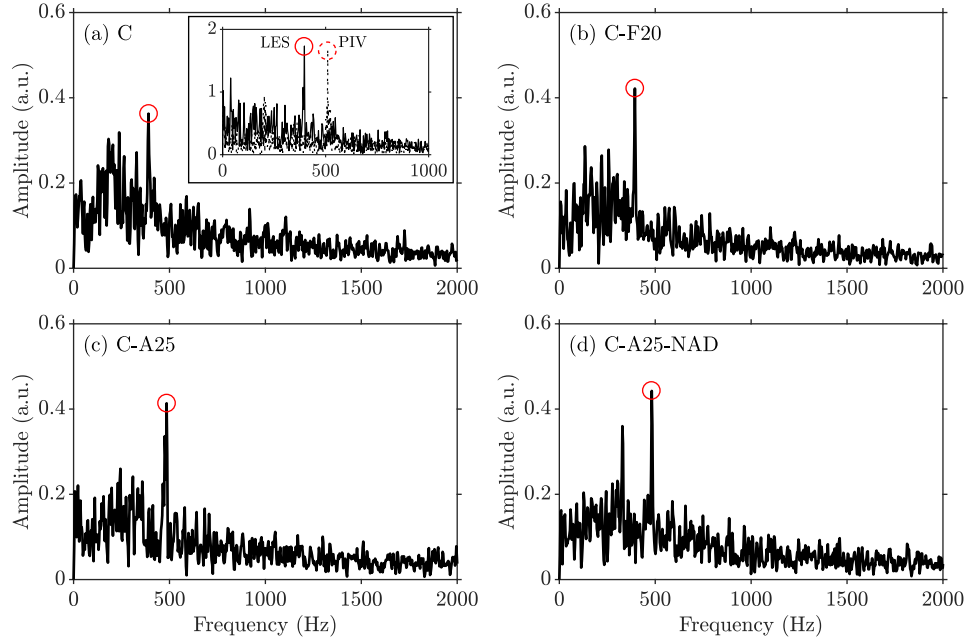


Fig. 5: Spectral behaviour of the azimuthal movement for the flame root using the azimuthal position fluctuations θ' for flames (a) C, (b) C-F20, (c) C-A25 and (d) C-A25-NAD. The inset of (a) shows the power spectral density signal of the axial velocity for a point located within the inner shear layer at $x = 13.5$ mm and $y = 9$ mm in the flame C simulation and the PIV measurements.

[23] that the spreading angle of the swirling flow in flame C is slightly over predicted, which is due to the flow separation along the contoured wall of the annular divergent air nozzle being delayed. This most likely causes the PVC frequency to be under predicted. This has also been observed in previous studies on a flame that has a higher global equivalence ratio and no thermo-acoustic instabilities present, referred to as flame A [21, 22]. A significantly finer grid is required to accurately capture the flow separation, which is not the aim of this work. It has been shown in the LES study by Chen et al. [22] that the PVC is the essential stabilisation mechanism and the spectral behaviour of the flame leading edge movement gives a frequency equal to the PVC frequency. The FFT of the azimuthal position fluctuations θ' about the mean on the transverse (y - z) plane is applied to the same

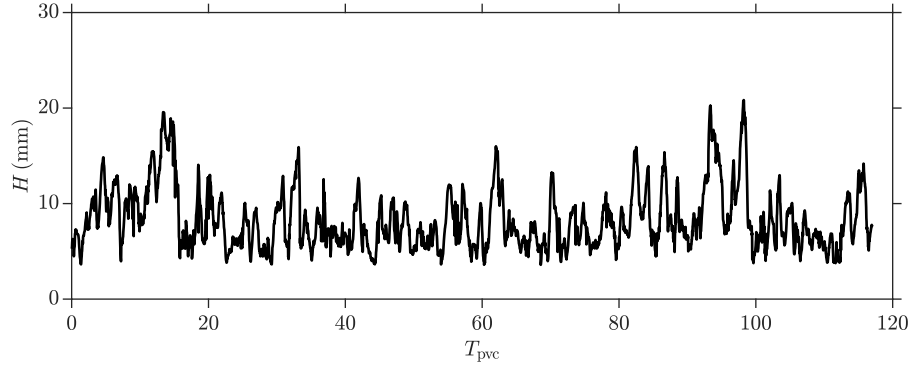


Fig. 6: Time series of the lift-off height above the fuel nozzle for flame C after the transient period from ignition $t_0 = 104$ ms.

four cases analysed in section 4.1 and these are shown in Fig. 5. For flame C, the FFT in Fig. 5a shows a peak that is at 390 Hz with an amplitude of 0.36. This amplitude is significantly lower than the peaks observed for flames A and B in the study by Chen et al. [22], which are not close to the lean blow-off limit. This peak frequency corresponds to a time period of $\tau_{pvc} = 2.56$ ms. As the air mass flow rate is the same for flame C-F20, the peak frequency is 394 Hz, as seen in Fig. 5b. For flames C-A25 and C-A25-NAD, the peak frequencies are seen to be 485 Hz and 482 Hz respectively, as shown in Figs. 5c and 5d. These frequencies are greater than those reported for flames C and C-F20 because the air flow rate is increased by 25 %.

Since the peaks and their corresponding frequencies for the four cases are consistent with the flow rates of each case, this suggests that the PVC is the dominant mechanism for the stabilisation of this flame and the azimuthal position of the flame follows the rotation of the PVC. However, there is significant low-frequency noise for the four cases, particularly for flames C and C-A25-NAD. Flame C is studied in further detail, since additional PLIF measurements are available for

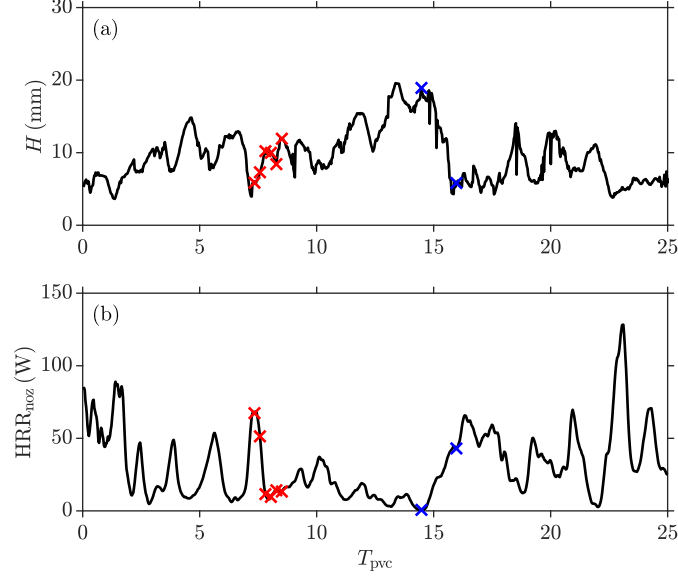


Fig. 7: Time series of the lift-off event for flame C showing (a) the lift-off height above the fuel nozzle and (b) the volume integrated heat release rate near the fuel nozzle region (CV1 in Fig. 4). The normalised time is $T_{pvc} = \hat{t}f_{pvc}$, where $\hat{t} = t - t_0$ and $t_0 = 104$ ms. The red crosses indicate the frames in Fig. 9a and the blue crosses represent the time interval for the analysis in Fig. 13.

validation of the observed local extinction and lift-off phenomena. A time series of the lift-off height for flame C is shown in Fig. 6 against a normalised time axis $T_{pvc} = \hat{t}f_{pvc}$, where $\hat{t} = t - t_0$ and the transient period from ignition is $t_0 = 104$ ms. In general, it is seen that the flame root fluctuates around its mean value of 8.32 mm. There are two short lift-off events at $T_{pvc} = 93$ and 98. Furthermore, it is shown in Fig. 6 that an extended lift-off event is present between $T_{pvc} = 7$ and 16. Two time series are shown for this lift-off event in Fig. 7a and 7b of the lift-off height and the volume integrated heat release rate within a volume of size $10 \times 20 \times 20 \text{ mm}^3$ around the nozzle region that is centred at $x = 0$; this volume is marked in Fig. 4 as CV1. It is shown in Fig. 7 that the flame experiences transients during the interval $2 \leq T_{pvc} \leq 7$, since the lift-off height increases and the nozzle integrated heat release rate periodically approaches zero with a pe-

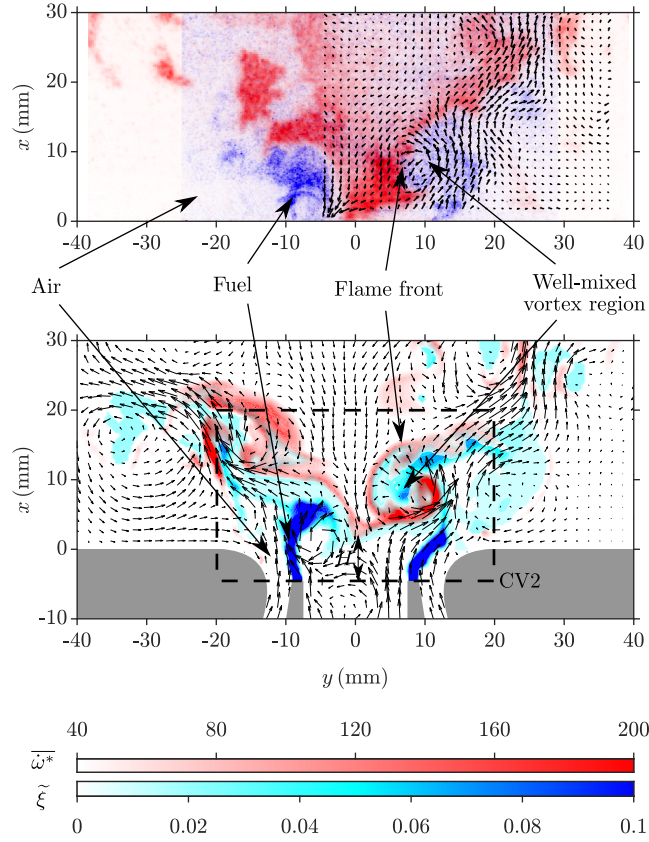


Fig. 8: Arbitrarily chosen snapshots of flame C showing the simultaneous PIV, and acetone- and OH-PLIF measurements (top) and the LES results of the velocity vectors, and the filtered reaction rate and mixture fraction (bottom). The colour bars are for the LES results. The control volume CV2 is used for the analysis in Fig. 18.

riod of $2 T_{\text{pvc}}$ and the maximum heat release rate is smaller than at the start of the sample. The flame is lifted between $T_{\text{pvc}} = 8$ and $T_{\text{pvc}} = 16$, since the integrated heat release rate in the nozzle region is small during this time interval.

It has been shown experimentally [5] and numerically [23] that local extinction occurs before a lift-off event. The flame lift-off event is triggered due to local extinction at the flame root, which is caused by the entrainment of inflammable mixtures into the region near the forward stagnation point of the IRZ. Although

this has been previously identified using OH-PLIF measurements [5], further insights into the lift-off event using acetone-PLIF are presented to understand the fuel–air mixing processes and their influence on local extinction events. An arbitrarily chosen snapshot with a stable flame is shown in Fig. 8. The measurements and LES results are shown respectively at the top and bottom of Fig. 8. The acetone-PLIF measurements are shown from white to blue, where regions of a strong blue colour denote pure fuel. The OH-PLIF measurements are shown from white to red and the flame front is located in the region where the colour changes from pale blue to red. For the LES snapshot, the mixture fraction within $0 < \tilde{\xi} < 0.1$ (white to blue) is plotted for mixtures that have progress variable values of $\tilde{c} < 0.5$, in order to represent the acetone-PLIF measurements. The flame is marked using the filtered reaction rate in the range $40 < \bar{\omega} < 200 \text{ kg/m}^3 \text{ s}$ (white to red).

As observed in the study by Stöhr et al. [15] using combined acetone- and OH-PLIF measurements, the PVC is known to pass through unmixed fuel and air. The PVC is crucial to flame stabilisation because it induces strong mixing of the unburnt fuel, air and hot products, which leads to ignition within these vortex structures. In Fig. 8, these are identified by the circular patterns of the velocity vectors and such regions have high vorticity magnitudes. In the LES snapshot in Fig. 8, a mixing region is developing at $x = 8 \text{ mm}$ and the flame is attached to the outer part of the structure. The fuel–air mixture is expected to be entrained into the centre of the vortex structure. Further downstream on the left-hand side, a reacting region is located at $x = 12 \text{ mm}$ with a flammable mixture, suggesting that the vortex is well-mixed and combustion is sustained.

It has been observed in the experimental study by Stöhr et al. [5] on flame C

that frequent extinction and re-ignition occurs over short time durations (< 1 ms). However, if this extinction persists for longer than the time required for one rotation of the PVC, then the flame lifts off. It has also been observed that local extinction must occur within the vortex structures along the inner shear layer to initiate the lift-off process. The measurements are used to identify when local extinction within the vortex structures occurs, since these give insights into the fuel–air mixing processes induced by the PVC and the subsequent flame roll-up process. The time series of the lift-off height and integrated heat release rate in the nozzle region in Fig. 7 are used to identify a lift-off event, as the nozzle heat release rate is low for the range $20 < \hat{t} < 40$ ms (approximately $T_{\text{pvc}} = 8$ to $T_{\text{pvc}} = 16$). There are oscillations in the nozzle heat release rate during the interval $2 \leq T_{\text{pvc}} \leq 7$. The last cycle is analysed, since the integrated heat release rate is small after this cycle and the lift-off height then increases. Snapshots of the simulations are shown in Fig. 9a at intervals of 0.6ms and the total duration of the sequence exceeds one PVC rotation period $\tau_{\text{pvc}} = 2.56$ ms. The selected PLIF images, shown in Fig. 9b, are 0.6ms apart and a time series of the integrated OH-PLIF signal is used to identify when the flame is lifted.

In the first frame in Fig. 9a at $\hat{t} = 18.825$ ms, the pale red colour close to the centre at $x = 8$ mm indicates the flame root region. The time series of the volume integrated heat release rate in the nozzle region at the first red point in Fig. 7b shows a lower value of 68 W compared to the maximum observed value of 128 W and with the observations in the first snapshot of Fig. 9a, it is demonstrated that the flame root is weak. This is also shown in the first PLIF image in Fig. 9b, as the OH-PLIF planar image signal is considerably weaker in comparison to Fig. 8. In the LES snapshot at $\hat{t} = 19.425$ ms, a vortex region is located at $x = 5$ mm near the

fuel jet at $y = -10$ mm and flame roll-up is present. At $x = 0$ mm and $y = 5$ mm, which is directly above the fuel jet, the top of a vortex is seen, as indicated by the

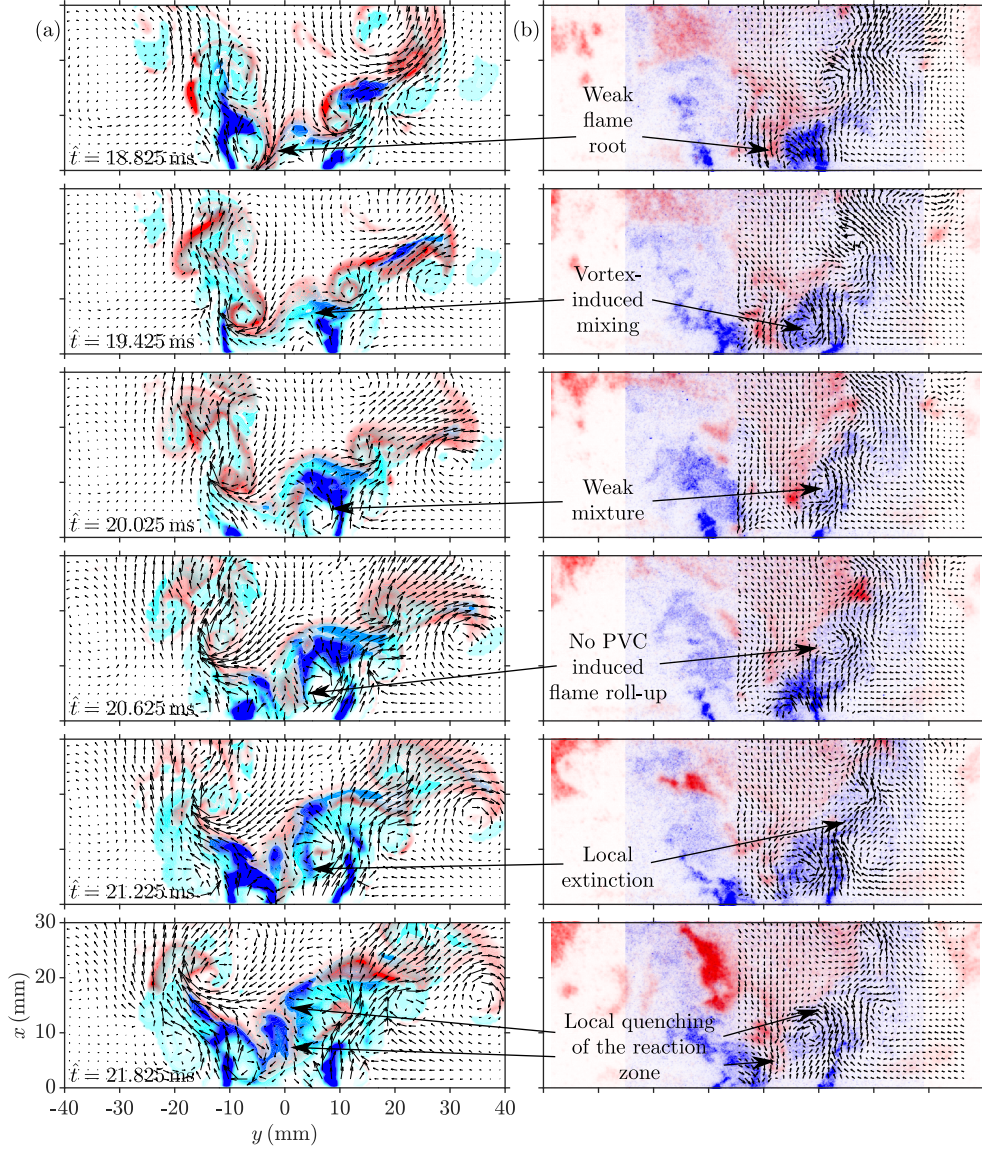


Fig. 9: Time series showing a local extinction event in the vortex from the (a) LES, and (b) the simultaneous PIV and PLIF measurements of flame C. The time for each frame is marked in Fig. 7 with red crosses and the duration of the sequence corresponds to $T_{pvc} = 1.17$. The LES snapshots use the same scales as shown in Fig. 8.

velocity vectors, and PVC induced mixing of the fuel and air is expected to occur. The next snapshot at $\hat{t} = 20.025$ ms shows the aforementioned vortex that is centred at $x = 5$ mm and $y = 8$ mm. It is shown that the mixture fraction is close to 0, as indicated by the white colour and this suggests that insufficient PVC induced mixing has occurred. This is also seen by the very pale blue colour in the corresponding acetone-PLIF image in Fig. 9b. A fuel-rich reacting mixture can be seen in Fig. 9a at $x = 5$ mm and $y = 2$ mm, which is due to the flame root igniting the PVC induced mixture. It is observed in the entire sequence of simultaneous PIV and PLIF measurements (not shown here) that the flame root ignites a well-mixed region within the vortex and leads to PVC induced flame roll-up, which must occur to keep the flame stable. However, the next snapshot at $\hat{t} = 20.625$ ms shows that the flame and its root have lower reaction rate values and no flame roll-up is seen. The flame is instead present further downstream and a flammable mixture located at $x > 20$ mm is ignited. In the snapshot at $\hat{t} = 21.225$ ms in Fig. 9a, it is seen there is no reacting mixture within the vortex because the fuel-air mixture is too lean and hence, no flame roll-up has occurred. This is referred to as a local extinction event. In addition, there is a pocket of a rich fuel-air mixture that is beyond the flammability limits at $x = 10$ mm and $y = -2$ mm, which is at the flame root region. This suggests that the PVC induced mixing on the left-hand side is weak and the variation of the mixture fraction in the flame root region is highly intermittent, which indicates a precursor to a lift-off event. The last snapshot in Fig. 9a shows local quenching of the reaction zone, as there is a very rich fuel-air mixture around the flame root region and the local reaction rates are lower. In addition, no reacting vortex structures can be seen. If there is PVC induced mixing, the absence of flame roll-up and the presence of fuel-rich mixtures in the flame

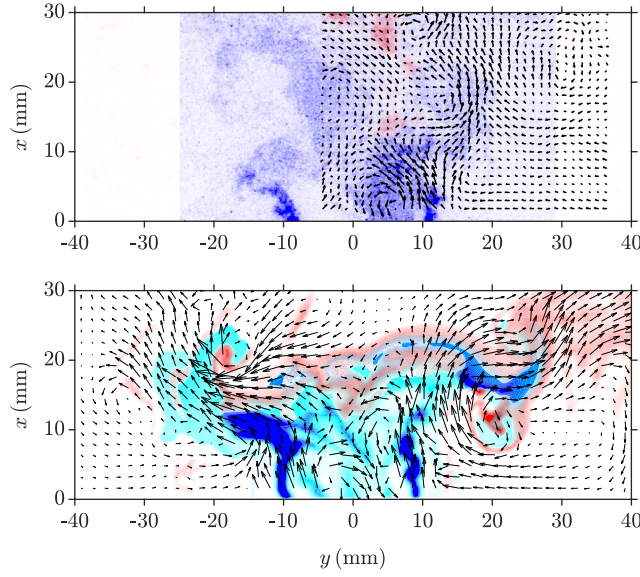


Fig. 10: Snapshots of flame C experiencing lift-off using the simultaneous PIV and PLIF measurements (top) and the simulation results (bottom). The LES results use the same scales as in Fig. 8.

root region for one PVC rotation period, then the flame experiences lift-off, as observed in the study by Stöhr et al. [5].

Figure 10 shows the flame at its maximum lift-off height at $T_{pvc} = 13.46$ in Fig. 7a. The velocity vectors in Fig. 10 from the experiment and the LES indicate that the opening angle of the IRZ is narrower in comparison to the stabilised flame shown in Figure 8. This is due to the absence of heat release and hot products around the typical flame root region. The measurements shown at the top of Fig. 10 indicate that the continuous supply of fuel and air pushes the flame root further downstream and the flame is known to stabilise at a downstream location outside of the measurement region, as seen with OH-PLIF measurements [5]. The measured lift-off event lasts for approximately 150 ms. For the simulation, the flame reaches a maximum lift-off height of approximately 19 mm above the fuel nozzle. Re-ignition around the flame root region is prevented, since PVC induced

mixing is also seen to be weak, since no vortices (circular patterns of the velocity vectors) can be identified. The flame is able to re-stabilise when sufficient mixing takes places between the fresh reactants and hot products near the fuel nozzle region. This occurs after approximately 20 ms in the simulation, as suggested by Fig. 6. As seen in the LES snapshot in Fig. 10, a flame is present at $x > 20$ mm and $y > 25$ mm and is stretched horizontally towards the walls. This is different in comparison to the experimental image, where OH zones only exist along the centreline. It is expected that reducing the global equivalence ratio and including non-adiabatic effects within the modelling should increase the duration of lift-off events. This is explored next.

4.3. *Effects of heat loss*

The comparisons in Fig. 4 show that the average flame lift-off heights are similar for all cases. Flames C-A25 and C-F20 stabilised closer to the fuel nozzle, whereas flame C-A25-NAD is positioned slightly further downstream in comparison to flame C. This behaviour is reflected in the lift-off height PDFs for these four cases in Fig. 11a; the PDF for flame C-NAD from the previous study [24] is also included. It is observed that the PDFs for flames C and C-A25 have similar shapes with peaks at approximately 6.5 mm. However, the PDF of flame C-A25 is shifted towards lower lift-off height values. For flame C-F20, the PDF is shifted towards higher lift-off height values, but the maximum values are similar to flame C-A25, which are less than the values for flame C. The PDFs for flames C-A25 and C-F20 are narrower in comparison to flame C, as the lift-off height does not exceed 15 mm, whereas the lift-off height is seen to be greater in the other cases. Figure 11b shows that the PDF of the heat release rate in the near-field of the nozzle region (CV1 in Fig. 4) is broader for flames C-A25 and C-F20, in comparison to

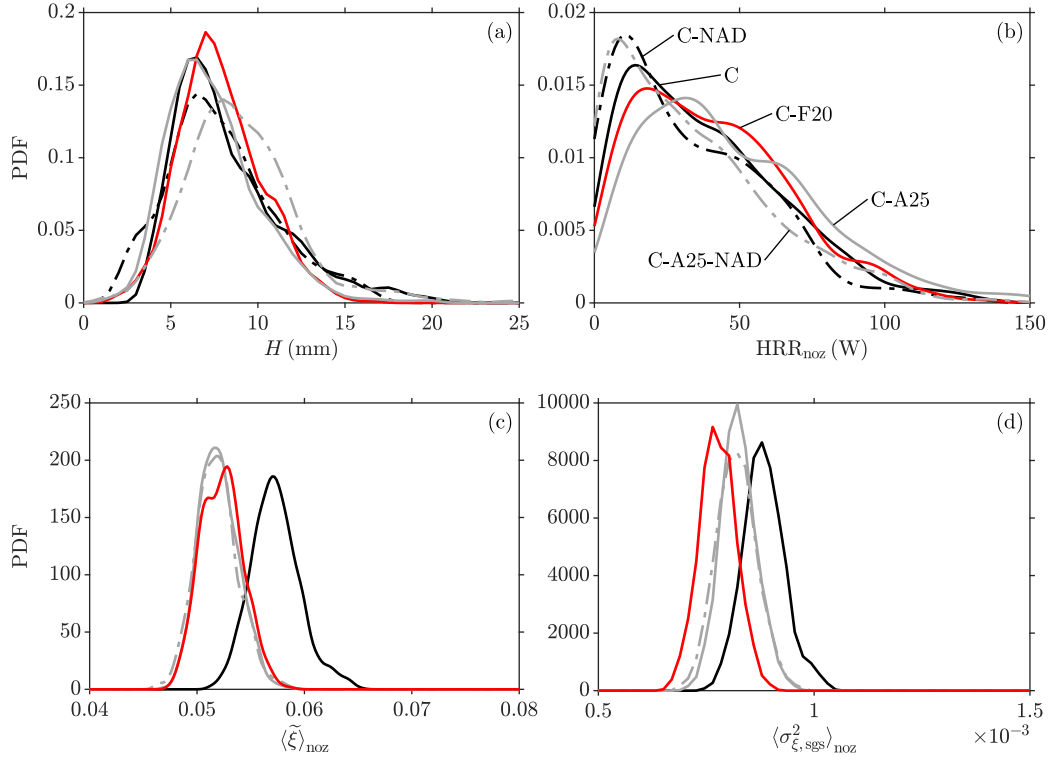


Fig. 11: Probability density functions of the (a) lift-off height, (b) integrated nozzle heat release rate, and the volume-averaged (c) mixture fraction and (d) mixture fraction sub-grid variance within the nozzle region across a 300 ms time sample.

flame C. This suggests that flames C-A25 and C-F20 stabilise closer to the fuel nozzle and are more stable.

The volume-averaged filtered mixture fraction and its sub-grid variance PDFs within the nozzle region (CV1 in Fig. 4) are shown in Figs. 11c and 11d respectively. It is seen that the mixture fraction PDF for flame C is at higher values than the cases with a lower global equivalence ratio. The PDFs of the other three cases are at lower values and the sub-grid variance is also decreased, as seen in Fig. 11d. Flame C-F20 has the lowest sub-grid variance, since the air flow rate is lower com-

pared to flames C-A25 and C-A25-NAD. The SGS variance is increased when the air flow rate is increased due to the stronger (and also faster rotating) PVC. As seen in Fig. 4 and by the heat release rate PDF in Fig. 11b, the flame is positioned closer to the fuel nozzle in flames C-A25 and C-F20, which is due to the fuel–air mixtures being leaner, as shown by the mixture fraction PDFs in Fig. 11c. The lift-off heights for flame C are observed to be similar when heat loss effects are included, as seen for the PDFs of flames C and C-NAD in Fig. 11a. The PDFs are similar for the nozzle heat release rate, but the peak values for flame C-NAD are lower, as seen in Fig. 11b. The sensitivity to heat loss effects is substantially higher when the global equivalence ratio is lowered. For flame C-A25-NAD, the lift-off height PDF covers higher values and the PDF of the heat release rate within the nozzle region is at lower values compared to flame C-NAD. The opposite behaviour is observed for flames C and C-A25 and this suggests that heat loss effects should be included within the combustion modelling framework to capture the unstable flame behaviour for flames approaching blow-off.

Analysis of the lift-off height time series for flame C-A25-NAD shows that a lift-off event occurs. Time series of the lift-off height and integrated heat release rate in the nozzle region for this lift-off event are shown in Fig. 12. The flame root reaches its maximum observed position during the interval $66 \leq T_{pvc} \leq 71$, whereas the maximum lift-off height is observed during the interval $10 \leq T_{pvc} \leq 14$ for flame C, as seen in Fig. 7. However, the flame root in flame C re-stabilises after approximately one rotation period of the PVC, whereas this process requires approximately four PVC rotation periods in flame C-A25-NAD. The inclusion of non-adiabatic flamelets causes the reaction rates to decrease and hence, the propagation speed of the flame is reduced for flame C-A25-NAD in comparison to

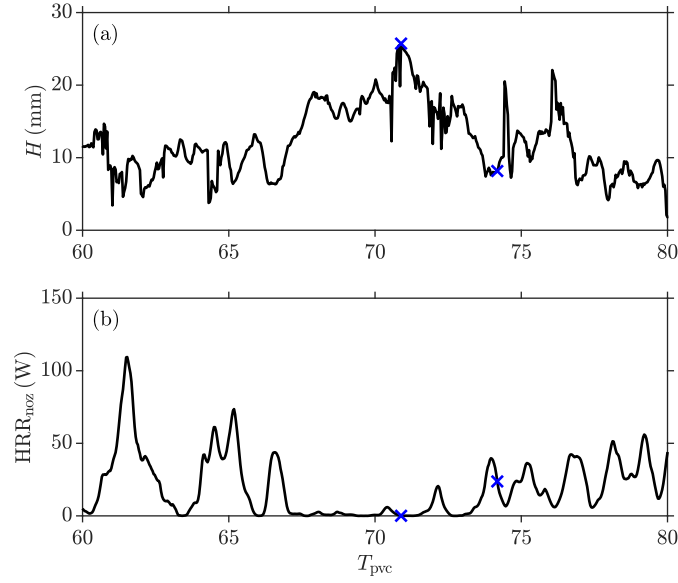


Fig. 12: Time series of the lift-off event for flame C-A25-NAD showing (a) the lift-off height above the fuel nozzle and (b) the volume integrated heat release rate near the fuel nozzle region (CV1 in Fig. 4). The normalised time is $T_{pvc} = \hat{t}f_{pvc}$, where $\hat{t} = t - t_0$ and $t_0 = 120$ ms. The blue crosses represent the analysis in Fig. 14.

flame C. Since no lift-off event is observed in flame C-A25, which has the same mass flow rates, including heat loss is important to capture the re-stabilisation process, since this process requires three more PVC rotation periods than as observed for flame C, as seen in Fig. 7.

The re-stabilisation processes are analysed for flames C and C-A25-NAD and these are shown in Figs. 13 and 14 respectively. The start and end times for this analysis are marked using blue crosses in Figs. 7 and 12 for flames C and C-A25-NAD respectively. The three-dimensional visualisation of the flame leading edge (based on the upstream point of the $\widetilde{T} = 1500$ K iso-surface above the fuel injectors) trajectory for flame C is shown in Fig. 13a and the top view is shown in Fig. 13b. It is shown that in the first interval of $14.5 \leq T_{pvc} \leq 14.8$, the flame leading edge is located at a radius of $r > 7$ mm and follows a circular arc in the

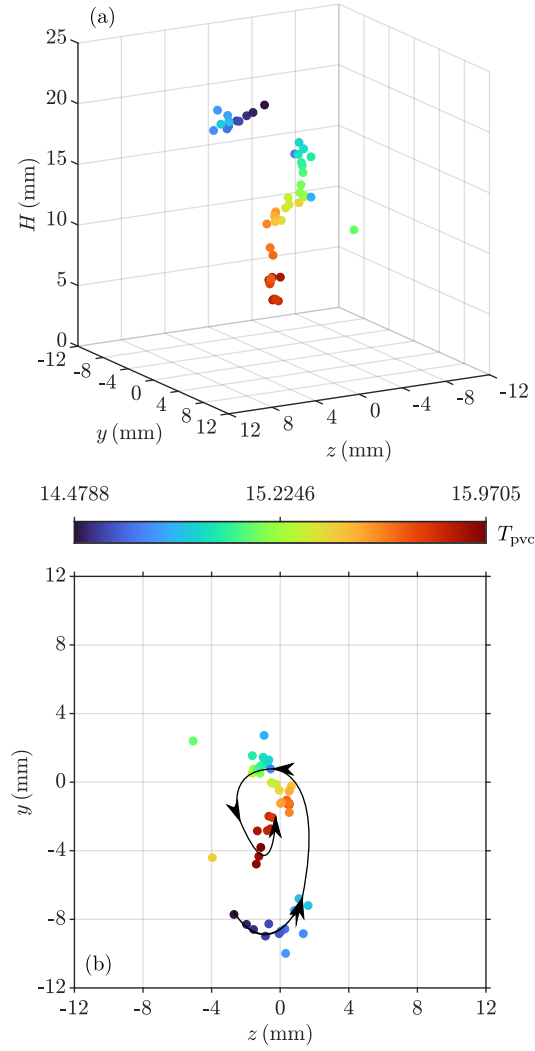


Fig. 13: Flame leading edge trajectory in (a) three-dimensional space and (b) top view during the re-stabilisation stage in flame C, as marked in Fig. 7.

same direction as the PVC. The flame leading edge then moves back and forth towards the centre and then the leading edge remains near the centre, as seen in Fig. 13b. As shown in Fig. 13a, the flame leading edge propagates upstream towards a lift-off height of approximately 6 mm after $T_{pvc} = 14.9$. This process requires approximately one PVC rotation period and the leading edge remains

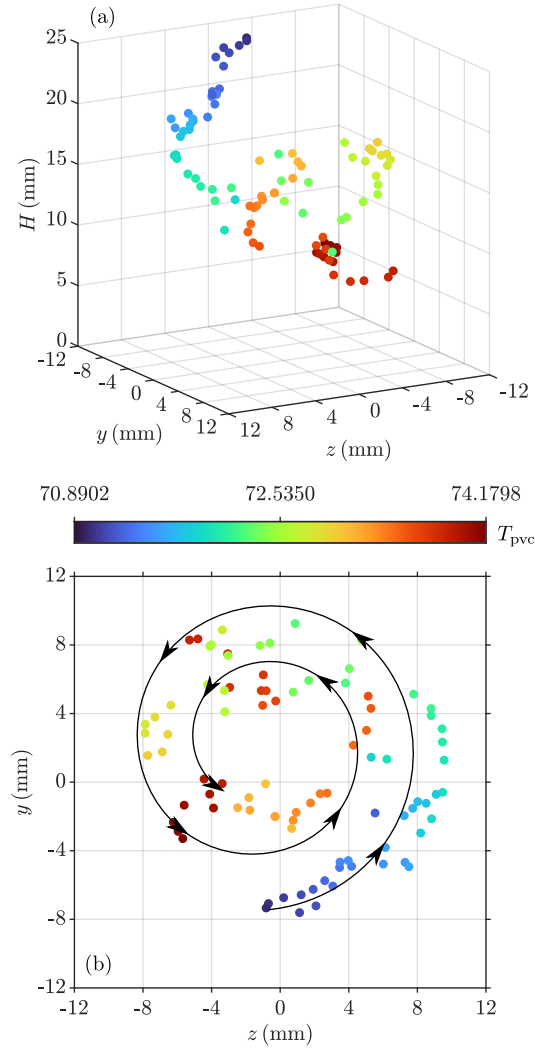


Fig. 14: Flame leading edge trajectory in (a) three-dimensional space and (b) top view during the re-stabilisation stage in flame C-A25-NAD, as marked in Fig. 12.

close to the centre.

The re-stabilisation process is different in flame C-A25-NAD as this process occurs over multiple rotations of the PVC, which is shown in Fig. 14. In general, it is shown that the flame root gradually approaches the centre with an azimuthal variation following the PVC rotation. This behaviour is not seen for flame C and

this further suggests that the flame leading edge paths are different because the propagation speed of the flame is reduced, due to heat losses in flame C-A25-NAD and the leading edge path is highly influenced by the PVC. It is shown in Fig. 14 that from $T_{pvc} = 70.9$ for one rotation period, the radial position of the flame leading edge remains in the region at a radius of 8 mm and its azimuthal position changes by 90° . The flame leading edge moves upstream by 8 mm during this stage. From $T_{pvc} = 72$, the azimuthal position of the leading edge changes by 1.5 rotations, as seen in Fig. 14b, which is equal to approximately 1.5 PVC rotation periods. This time period is observed to be the same for flame C-NAD, as observed previously in the study by Massey et al. [24]. This suggests that the re-stabilisation process is highly influenced by the dynamics of the PVC. This is not seen in flame C because the chemical time scales are shorter in comparison to the PVC time scale (see Fig. 18), as adiabatic flamelets are used for the reaction rate source term. Hence, heat loss effects must be included at the flamelet level for the simulation of flames near or approaching the blow-off condition.

4.4. *Blow-off correlation analysis*

The interactions between the flow and chemical time scales for flames approaching blow-off can be characterised using dimensionless parameters, such as the Damköhler number $Da = \tau_f/\tau_c$, which is the ratio of a turbulent flow time scale τ_f to a chemical time scale τ_c [56]. Correlations that are based on the Damköhler number have been proposed and applied to different burner configurations to characterise blow-off. A correlation for blow-off in turbulent premixed flames has been proposed by Radhakrishnan et al. [57] and has been applied to swirl-stabilised bluff body flames in the study by Cavaliere et al. [16]. This corre-

lation is written as

$$\frac{1}{Da} = \left(\frac{U_b}{D} \frac{\nu}{(s_L)^2} \right)^{1/2} > R, \quad (5)$$

where U_b is a bulk-mean velocity at the entry to the combustion chamber, D is the bluff body diameter, R is a constant representing the limit for blow-off correlation for the burner, and ν and s_L are the kinematic viscosity and the laminar flame speed respectively for a stoichiometric fuel–air mixture. The values for the correlation in Eq. (5) are within $0.87 \leq 1/Da \leq 1.34$ for the swirl-stabilised bluff body flames studied by Cavaliere et al. [16].

This correlation is applied to the present case with more complex flow fields, since air enters the combustion chamber through central and annular passages with swirlers. Using the inner and outer diameters of the annular nozzle, the value of $1/Da$ is 0.36 for flame C. This value is the same for flame C-F20, as the bulk air flow rate is the same, whereas the value of $1/Da$ for flame C-A25 is 0.40. The limitation with this correlation is that it does not change when the global equivalence ratio is decreased by changing the fuel mass flow rates for a given air mass flow rate. Moreover, it is based on the bulk flow characteristics and geometrical parameters of a simpler flow configuration. The sensitivity of this correlation to the operating conditions of the flames is small.

The study by Ciardiello et al. [58] applied this correlation to a multi-burner configuration and it is shown that the correlation cannot capture the blow-off limits, since the burner exhibits more complex phenomena related to the interaction between adjacent flames. Blow-off correlations have been developed to characterise blow-off limits for non-premixed unconfined jet flames [50, 59]. In addition, correlations have been used for non-premixed configurations that contain co-axial air and fuel streams with non-swirling flows [60] and with swirling

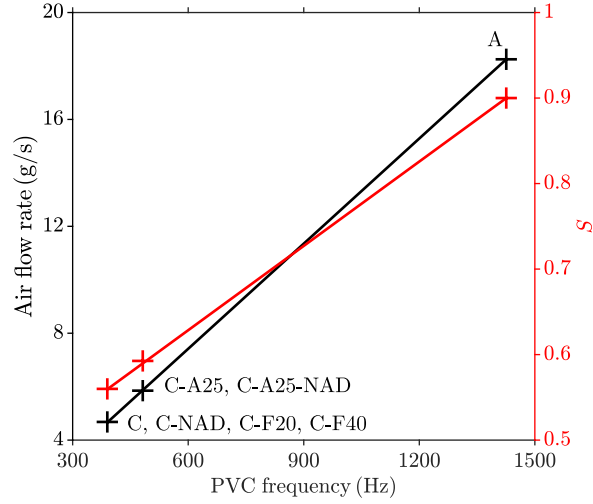


Fig. 15: Computed PVC frequencies as functions of the air mass flow rate and the swirl number S . The symbols represent the simulation results.

flows [61]. Each configuration requires a different correlation, since the blow-off limits in the aforementioned studies are substantially different; these are reviewed by Shanbhogue et al. [4] and Driscoll [62]. Hence, care must be taken when applying these correlations to different burners.

It has been shown in sections 4.2 and 4.3 that the PVC plays crucial role in flame stabilisation mechanism. Hence, the time scale of its rotation is chosen to be the flow time scale $\tau_{pvc} = 1/f_{pvc}$ and the Damköhler number for this case is defined as $Da = \tau_{pvc}/\tau_c$ [20] with the chemical time scale $\tau_c = \bar{\rho}/\bar{\omega}$. Figure 15 shows the PVC frequency as a function of the air mass flow rate and the swirl number. The swirl number is given as [63]

$$S = \frac{\int_0^R \rho U U_\theta r^2 dr}{R \int_0^R \rho U^2 r dr}, \quad (6)$$

where U and U_θ are the axial and azimuthal velocities respectively. The swirl

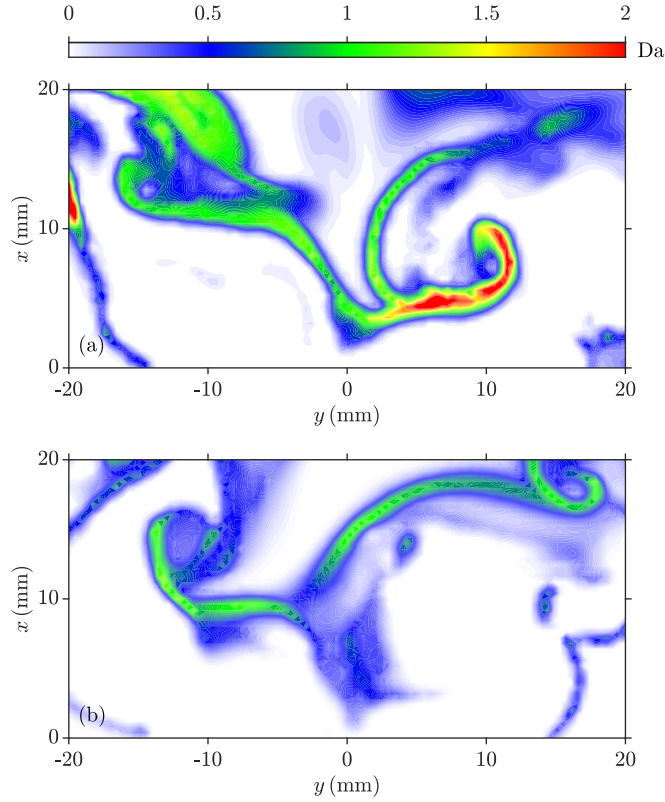


Fig. 16: Snapshots of $Da = \tau_{pvc}/\tau_c$ when flame C is (a) stabilised (the same snapshot as Fig. 8) and (b) before the lift-off event (the fourth snapshot in Fig. 9a).

number for this case is calculated following the previous experimental studies [12]. The results for flame A, observed to be stable with $\phi_{glob} = 0.65$, are obtained from the study by Chen et al. [22]. It is seen that the PVC frequency increases linearly with the air mass flow rate and this has also been reported in the experimental study by Stöhr et al. [19] and in other studies [3, 64–66].

Snapshots of the local Da values when the flame is stabilised and just prior to lift-off are shown in Fig. 16 and 17 for flames C and C-A25-NAD respectively. These are shown to identify values of Da in the regions of local extinction. The value of τ_{pvc} is the critical time period that leads to lift-off, since it is observed in

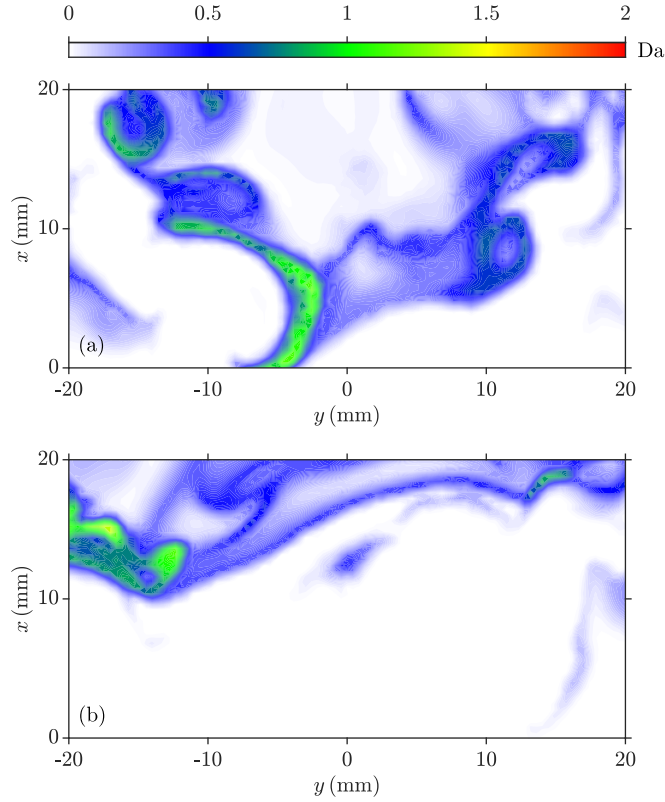


Fig. 17: Snapshots of $Da = \tau_{pvc}/\tau_c$ when flame C-A25-NAD is (a) stabilised and (b) before the lift-off event ($T_{pvc} = 67.6$ in Fig. 12).

the study by Stöhr et al. [5] that lift-off occurs if local extinction and quenching of the flame root simultaneously occur during this period, and this is influenced by the PVC. Local extinction is a prelude to flame blow-off [4] and is observed in all cases. However, local extinction must occur continuously across this time period and it is influenced locally by the PVC. The frequency of the PVC and its rotation period are not local and are influenced by global parameters, such as the mass flow rate, swirl number and the geometry of the annular divergent air nozzle. This time scale is chosen as the flow time scale to correlate local extinction, since the PVC is the stabilisation mechanism for this configuration. The values of Da

are larger than unity in regions with strong reactivity and this is seen in the flame root region when the flame is stabilised, as shown in Fig. 16a. The values of Da decrease substantially below one when the flame starts to lift-off and suggests that the flame root becomes weak (see Fig. 9a), as shown in Fig. 16b. This is also seen in regions of the flame and on the right-hand side of the flame root, which is the region where failed PVC flame roll-up is identified, as shown in Fig. 9a, and values of Da in this region are below 0.25. Similar snapshots are shown for flame C-A25-NAD in Fig. 17. It is seen that the flame root has values of Da around unity and the values within the flame and vortices are within the range $0.6 < Da < 1$ when the flame is stabilised, as seen in Fig. 17a. However, the right-hand side of the flame root shows a weaker flame with $Da < 0.5$. The flame is also seen to be weak in Fig. 17b, where $Da < 0.3$. For the snapshots shown, the PVC and chemical time scales are of the same order of magnitude and the interactions between the PVC and the flame are closely coupled, since it is observed for this case that the flame is weaker when $Da < 0.5$ and prone to local extinction when $Da < 0.25$.

The PDFs of the Damköhler number and the chemical time scales are shown in Fig. 18 when the flame is stabilised. These are shown to identify the time scale range for each case. The volume chosen for data sampling to construct these PDFs is from the nozzle up to a streamwise location of $x = 20$ mm and within a radius of 20 mm, since the flame stabilises within this region and the flame–vortex interactions are present; this control volume is marked in Fig. 8 and labelled as CV2. For the simulations listed in Table 1, the PDFs for flames C, C-A25, C-A25-NAD and C-F40 are analysed, since significant differences are seen among these four cases. It is shown in Fig. 18b that the PDF for flame C is between flames C-A25

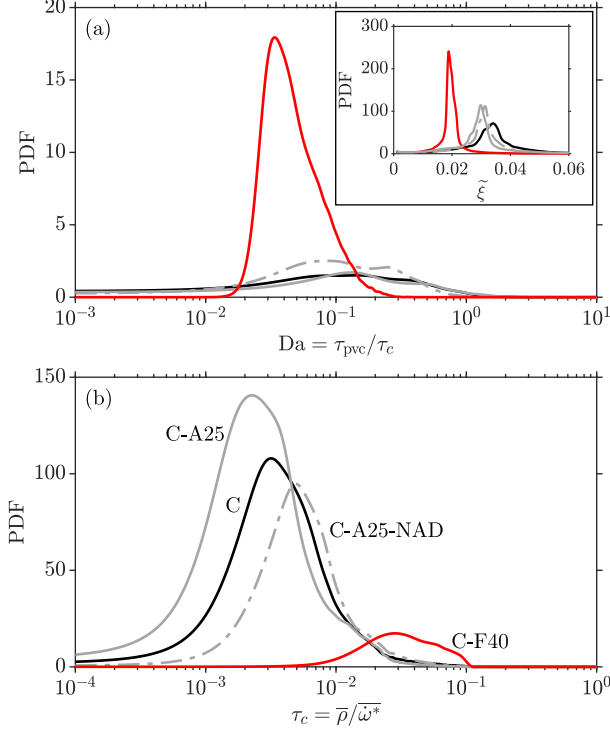


Fig. 18: Probability density functions of (a) Da and (b) τ_c in the simulations for an arbitrary time whereby the flame is stabilised within the control volume CV2, as marked in Fig. 8. The inset of (a) shows the filtered mixture fraction PDF within CV2. The time chosen for flame C is the same as in Fig. 8.

and C-A25-NAD, where flame C-A25-NAD has the longest chemical time scales in these three cases. This further suggests that including heat loss is important, since the inset of Fig. 18a shows that the mixture fraction is smaller in flames C-A25 and C-A25-NAD than in flame C. The PDFs of the Damköhler are similar for flames C and C-A25. This is because flame C-A25 has a shorter PVC time scale, but also shorter chemical time scales, as seen in Fig. 18b. The PDF for flame C-A25-NAD has lower values of Da because the chemical time scales are longer, which implies this case is more unstable and prone to local extinction. The averaged chemical time scale $\langle \tau_c \rangle$ within CV2 for each PDF is obtained and

Case	f_{pvc} (Hz)	$\langle \tau_c \rangle = \langle \bar{\rho} / \bar{\omega} \rangle$ (s)	$\langle \text{Da} \rangle = \tau_{\text{pvc}} / \langle \tau_c \rangle$	$(\delta_L^0 / s_L^0)_{\langle \phi \rangle}$ (s)
C [23]	390	0.013	0.20	0.0027
C-NAD [24]	390	0.015	0.17	0.0047
C-F20	394	0.013	0.20	0.0051
C-F40	394	0.048	0.05	-
C-A25	485	0.009	0.22	0.0046
C-A25-NAD	482	0.014	0.15	0.0058

Table 2: Frequency of the PVC, first moment of the chemical time scale PDF in Fig. 18 and the average Damköhler number for the simulations listed in Tab. 1.

these are shown in Table 2. The average Damköhler number $\langle \text{Da} \rangle = \tau_{\text{pvc}} / \langle \tau_c \rangle$ is calculated and these are also listed in Table 2. Flame C-A25-NAD has the lowest value of $\langle \text{Da} \rangle$ in the cases analysed thus far, suggesting that this case is the most unstable and closest to blow-off, which is consistent with the observations in section 4.3. It is mentioned in section 4.1 that flame C-F40 did not stabilise after ignition and the PDFs of an instant during this event are shown in Fig. 18. The chemical time scale PDF for flame C-F40 is shifted towards larger values of the chemical time scale and the peak of the PDF for Da decreases by approximately an order of magnitude. The average value of $\langle \text{Da} \rangle$ of flame C-F40 is 0.05. As indicated by the values of $\langle \text{Da} \rangle$, the critical Damköhler number Da^* is within the values for flames C-A25-NAD and C-F40. Therefore, a blow-off correlation can be written in a similar form as the correlation shown in Eq. (5) as

$$\frac{1}{\langle \text{Da} \rangle} \sim f_{\text{pvc}} \langle \tau_c \rangle \geq \frac{1}{\text{Da}^*} \quad (7)$$

The correlation shown in Eq. (7) is in a simple form, but since this configuration is more complex, both time scales are sensitive to various parameters.

The flow time scale τ_{pvc} is sensitive to the bulk flow velocity, swirl number and the geometry, as these affect the recirculation zone structure [67] and the PVC frequency [64]. Obtaining a chemical time scale is more challenging with experimental measurements, since the heat release rate and reaction rate are not readily available. Therefore, chemical time scales based on bulk properties are preferred, which typically include the laminar flame speed and flame thickness. Since the mixture fraction varies locally within the flame in this configuration, using a bulk chemical time scale based on the global equivalence ratio is not correct (e.g. δ_L^0/s_L^0). It is attempted to calculate δ_L^0/s_L^0 using the first moment of the mixture fraction PDF shown in the inset of Fig. 18a to get the corresponding equivalence ratio $\langle\phi\rangle$ and finding the value of $(\delta_L^0/s_L^0)_{\langle\phi\rangle}$. These values are listed in Table 2 and the effects of heat loss are included for flames C-NAD and flame C-A25-NAD by using the mean normalised enthalpy. As expected, the values of $(\delta_L^0/s_L^0)_{\langle\phi\rangle}$ increase for the cases where the global equivalence ratios are lower. The values of $(\delta_L^0/s_L^0)_{\langle\phi\rangle}$ are also higher for the cases containing heat loss effects. It is seen in Table 2 that the value for flame C-F40 could not be determined because its mean equivalence ratio from the mixture fraction PDF in Fig. 18a is below the lean flammability limit. However, the simulation shows that although failed ignition is observed, a weak flame is still present. This also demonstrates why a global chemical time scale is not suitable for this case, as it does not account for the local reacting regions. In addition, it is shown that including heat loss affects the values of $(\delta_L^0/s_L^0)_{\langle\phi\rangle}$ and it is demonstrated in this work that heat loss modelling is important to consider for flames approaching blow-off. This makes obtaining a chemical time scale more challenging, since the amount of heat loss cannot be estimated *a priori*. More simulations would need to be undertaken at different

global equivalence ratios and mass flow rates (and hence, swirl numbers) in order to determine the behaviour of these time scales approaching blow-off.

5. Concluding remarks

Large eddy simulations of swirl-stabilised flames in a GTMC gradually approaching lean blow-off are undertaken. These flames approach lower global equivalence ratios, which is achieved by increasing and decreasing the air and fuel flow rates respectively. A presumed joint PDF approach with unstrained premixed flamelets and tabulated chemistry is used for SGS combustion modelling. The mixture fraction and progress variable are used to prescribe the local thermochemical states in partially premixed flames. The normalised enthalpy is included in the joint PDF to introduce heat loss effects within the combustion modelling. Analysis of the time-averaged fields shows that the IRZ volume is increased when the global equivalence ratio is decreased. The time-averaged flame base is closer to the fuel nozzle for the two cases with the lower global equivalence ratio that use adiabatic flamelets, which is confirmed by the averaged values of the volume integrated heat release rate near the fuel nozzle. Comparisons between the computational results, and the PIV and PLIF measurements for the baseline case, referred to as flame C, show that the mechanisms leading to local extinction are well captured in the simulation. Insufficient PVC induced mixing of the fuel, air and hot products is observed to be the main mechanism for local extinction before the lift-off event. Further analysis of the simulations shows that including heat loss effects within the modelling is important for flames near or approaching blow-off. Simulations with the adiabatic flamelet model show that the flames with lower global equivalence ratios stabilised closer to the fuel nozzle. However, the non-

adiabatic simulation with a lower global equivalence ratio shows that the flame is more unstable and a lift-off event is captured. It is also seen that the re-stabilisation of the flame root when the flame is lifted occurs over several PVC rotations in the non-adiabatic simulation, whereas flame C re-stabilised after one rotation. This is attributed to the adiabatic flamelet model over predicting the propagation speed of the flame, since the local filtered reaction rates are higher. The simulations are used to propose a blow-off correlation based on the Damköhler number. The flow time scale is based on the PVC rotation period and the chemical time scale uses the local filtered reaction rate and density. It is demonstrated that the simulations have low Damköhler numbers and the non-adiabatic flamelet simulation with a lower global equivalence ratio has the lowest Damköhler number for the flames that stabilised. A simulation with failed ignition is used to qualitatively indicate a critical Damköhler number for blow-off. It is of interest to quantitatively find limits for the correlation and to explore using geometrical and thermochemical information to represent the chemical time scale, but additional simulations are needed at higher swirl numbers (or higher air flow rates) at different global equivalence ratios.

Acknowledgements

J. C. Massey acknowledges the financial support from the EPSRC provided through a doctoral training award (grant number RG80792). J. C. Massey, Z. X. Chen and N. Swaminathan acknowledge the financial support from Mitsubishi Heavy Industries, Ltd., Takasago, Japan. This work used the ARCHER UK National Supercomputing Service (<https://www.archer.ac.uk>). The authors are grateful to the EPSRC (grant number EP/R029369/1) and ARCHER for financial and

computational support as a part of their funding to the UK Consortium on Turbulent Reacting Flows (<https://www.ukctrf.com>). The computational resources provided by the EPSRC through a resource allocation panel award (e620) are also acknowledged.

References

- [1] D. Feikema, R.-H. Chen, J. F. Driscoll, Blowout of nonpremixed flames: Maximum coaxial air velocities achievable, with and without swirl, *Combust. Flame* 86 (1991) 347–358.
- [2] N. Syred, N. A. Chigier, J. M. Beér, Flame stabilization in recirculation zones of jets with swirl, *Symp. (Int.) Combust.* 13 (1971) 617–624.
- [3] D. G. Lilley, Swirl Flows in Combustion: A Review, *AIAA J.* 15 (1977) 1063–1078.
- [4] S. J. Shanbhogue, S. Husain, T. C. Lieuwen, Lean blowoff of bluff body stabilized flames: Scaling and dynamics, *Prog. Energy Combust. Sci.* 35 (2009) 98–120.
- [5] M. Stöhr, I. Boxx, C. Carter, W. Meier, Dynamics of lean blowout of a swirl-stabilized flame in a gas turbine model combustor, *Proc. Combust. Inst.* 33 (2011) 2953–2960.
- [6] N. Syred, V. I. Hanby, A. K. Gupta, Resonant Instabilities Generated by Swirl Burner, *J. Inst. Fuel* 43 (1973) 402–407.

- [7] N. Syred, A review of oscillation mechanisms and the role of the precessing vortex core (PVC) in swirl combustion systems, *Prog. Energy Combust. Sci.* 32 (2006) 93–161.
- [8] N. Syred, N. A. Chigier, J. M. Beér, The damping of precessing vortex cores by combustion in swirl generators, *Astronaut. Acta* 17 (1972) 783–801.
- [9] N. Syred, A. K. Gupta, J. M. Beér, Temperature and density gradient changes arising with the precessing vortex core and vortex breakdown in swirl burners, *Symp. (Int.) Combust.* 15 (1975) 587–597.
- [10] L. Selle, G. Lartigue, T. Poinso, R. Koch, K.-U. Schildmacher, W. Krebs, B. Prade, P. Kaufmann, D. Veynante, Compressible large eddy simulation of turbulent combustion in complex geometry on unstructured meshes, *Combust. Flame* 137 (2004) 489–505.
- [11] W. Meier, X. R. Duan, P. Weigand, Reaction zone structures and mixing characteristics of partially premixed swirling CH₄/air flames in a gas turbine model combustor, *Proc. Combust. Inst.* 30 (2005) 835–842.
- [12] P. Weigand, W. Meier, X. R. Duan, W. Stricker, M. Aigner, Investigations of swirl flames in a gas turbine model combustor: I. Flow field, structures, temperature, and species distributions, *Combust. Flame* 144 (2006) 205–224.
- [13] W. Meier, X. R. Duan, P. Weigand, Investigations of swirl flames in a gas turbine model combustor: II. Turbulence-chemistry interactions, *Combust. Flame* 144 (2006) 225–236.

- [14] D. Galley, S. Ducruix, F. Lacas, D. Veynante, Mixing and stabilization study of a partially premixed swirling flame using laser induced fluorescence, *Combust. Flame* 158 (2011) 155–171.
- [15] M. Stöhr, C. M. Arndt, W. Meier, Transient effects of fuel-air mixing in a partially-premixed turbulent swirl flame, *Proc. Combust. Inst.* 35 (2015) 3327–3335.
- [16] D. E. Cavaliere, J. Kariuki, E. Mastorakos, A Comparison of the Blow-Off Behaviour of Swirl-Stabilized Premixed, Non-Premixed and Spray Flames, *Flow Turbul. Combust.* 91 (2013) 347–372.
- [17] H. Zhang, E. Mastorakos, Prediction of Global Extinction Conditions and Dynamics in Swirling Non-premixed Flames Using LES/CMC Modelling, *Flow Turbul. Combust.* 96 (2016) 863–889.
- [18] P. C. Ma, H. Wu, J. W. Labahn, T. Jaravel, M. Ihme, Analysis of transient blow-out dynamics in a swirl-stabilized combustor using large-eddy simulations, *Proc. Combust. Inst.* 37 (2019) 5073–5082.
- [19] M. Stöhr, I. Boxx, C. D. Carter, W. Meier, Experimental study of vortex-flame interaction in a gas turbine model combustor, *Combust. Flame* 159 (2012) 2636–2649.
- [20] M. Stöhr, C. M. Arndt, W. Meier, Effects of Damköhler number on vortex-flame interaction in a gas turbine model combustor, *Proc. Combust. Inst.* 34 (2013) 3107–3115.

- [21] Z. X. Chen, N. Swaminathan, M. Stöhr, W. Meier, Interaction between self-excited oscillations and fuel-air mixing in a dual swirl combustor, *Proc. Combust. Inst.* 37 (2019) 2325–2333.
- [22] Z. X. Chen, I. Langella, N. Swaminathan, M. Stöhr, W. Meier, H. Kolla, Large Eddy Simulation of a dual swirl gas turbine combustor: Flame/flow structures and stabilisation under thermoacoustically stable and unstable conditions, *Combust. Flame* 203 (2019) 279–300.
- [23] J. C. Massey, Z. X. Chen, N. Swaminathan, Lean Flame Root Dynamics in a Gas Turbine Model Combustor, *Combust. Sci. Technol.* 191 (2019) 1019–1042.
- [24] J. C. Massey, Z. X. Chen, N. Swaminathan, Modelling Heat Loss Effects in the Large Eddy Simulation of a Lean Swirl-Stabilised Flame, *Flow Turbul. Combust.* 106 (2021) 1355–1378.
- [25] P. Palies, T. Schuller, D. Durox, L. Y. M. Gicquel, S. Candel, Acoustically perturbed turbulent premixed swirling flames, *Phys. Fluids* 23 (2011) 037101.
- [26] R. Mercier, P. Auzillon, V. Moureau, N. Darabiha, O. Gicquel, D. Veynante, B. Fiorina, LES modeling of the impact of heat losses and differential diffusion on turbulent stratified flame propagation: Application to the TU Darmstadt stratified flame, *Flow Turbul. Combust.* 93 (2014) 349–381.
- [27] P. Benard, G. Lartigue, V. Moureau, R. Mercier, Large-Eddy Simulation of the lean-premixed PRECCINSTA burner with wall heat loss, *Proc. Combust. Inst.* 37 (2019) 5233–5243.

- [28] S. B. Pope, *Turbulent Flows*, Cambridge University Press, Cambridge, UK, 2000.
- [29] J. Smagorinsky, General Circulation Experiments with the Primitive Equations, *Mon. Weather Rev.* 91 (1963) 99–164.
- [30] Z. Chen, S. Ruan, N. Swaminathan, Large Eddy Simulation of flame edge evolution in a spark-ignited methane-air jet, *Proc. Combust. Inst.* 36 (2017) 1645–1652.
- [31] D. Bradley, P. H. Gaskell, A. K. C. Lau, A mixedness-reactedness flamelet model for turbulent diffusion flames, *Symp. (Int.) Combust.* 23 (1990) 685–692.
- [32] R. W. Bilger, The structure of turbulent nonpremixed flames, *Symp. (Int.) Combust.* 22 (1988) 475–488.
- [33] Z. X. Chen, I. Langella, R. S. Barlow, N. Swaminathan, Prediction of local extinctions in piloted jet flames with inhomogeneous inlets using unstrained flamelets, *Combust. Flame* 212 (2020) 415–432.
- [34] C. D. Pierce, P. Moin, A dynamic model for subgrid-scale variance and dissipation rate of a conserved scalar, *Phys. Fluids* 10 (1998) 3041–3044.
- [35] H. Pitsch, Large-Eddy Simulation of Turbulent Combustion, *Annu. Rev. Fluid Mech.* 38 (2006) 453–482.
- [36] T. D. Dunstan, Y. Minamoto, N. Chakraborty, N. Swaminathan, Scalar dissipation rate modelling for large eddy simulation of turbulent premixed flames, *Proc. Combust. Inst.* 34 (2013) 1193–1201.

- [37] N. Swaminathan, K. N. C. Bray, Effect of dilatation on scalar dissipation in turbulent premixed flames, *Combust. Flame* 143 (2005) 549–565.
- [38] P. Domingo, L. Vervisch, K. Bray, Partially premixed flamelets in LES of nonpremixed turbulent combustion, *Combust. Theory Model.* 6 (2002) 529–551.
- [39] K. Bray, P. Domingo, L. Vervisch, Role of the progress variable in models for partially premixed turbulent combustion, *Combust. Flame* 141 (2005) 431–437.
- [40] S. Ruan, N. Swaminathan, O. Darbyshire, Modelling of turbulent lifted jet flames using flamelets: A priori assessment and a posteriori validation, *Combust. Theory Model.* 18 (2014) 295–329.
- [41] D. G. Goodwin, H. K. Moffat, R. L. Speth, *Cantera: An Object-oriented Software Toolkit for Chemical Kinetics, Thermodynamics, and Transport Processes*, <https://www.cantera.org>, 2017.
- [42] F. Proch, A. M. Kempf, Modeling heat loss effects in the large eddy simulation of a model gas turbine combustor with premixed flamelet generated manifolds, *Proc. Combust. Inst.* 35 (2015) 3337–3345.
- [43] J. C. Massey, *Analyses of Bluff Body and Swirl-Stabilised Flames Using Large Eddy Simulation*, Ph.D. thesis, University of Cambridge, 2019.
- [44] A. Yoshizawa, K. Horiuti, A Statistically-Derived Subgrid-Scale Kinetic Energy Model for the Large-Eddy Simulation of Turbulent Flows, *J. Phys. Soc. Japan* 54 (1985) 2834–2839.

- [45] F. Nicoud, F. Ducros, Subgrid-Scale Stress Modelling Based on the Square of the Velocity Gradient Tensor, *Flow Turbul. Combust.* 62 (1999) 183–200.
- [46] J. C. Massey, I. Langella, N. Swaminathan, A scaling law for the recirculation zone length behind a bluff body in reacting flows, *J. Fluid Mech.* 875 (2019) 699–724.
- [47] L. Vanquickenborne, A. van Tiggelen, The stabilization mechanism of lifted diffusion flames, *Combust. Flame* 10 (1966) 59–69.
- [48] N. Peters, F. A. Williams, Liftoff characteristics of turbulent jet diffusion flames, *AIAA J.* 21 (1983) 423–429.
- [49] W. M. Pitts, Assessment of theories for the behavior and blowout of lifted turbulent jet diffusion flames, *Symp. (Int.) Combust.* 22 (1988) 809–816.
- [50] J. E. Broadwell, W. J. A. Dahm, M. G. Mungal, Blowout of turbulent diffusion flames, *Symp. (Int.) Combust.* 20 (1984) 303–310.
- [51] S. F. Ahmed, E. Mastorakos, Spark ignition of lifted turbulent jet flames, *Combust. Flame* 146 (2006) 215–231.
- [52] J. C. Massey, Z. X. Chen, N. Swaminathan, Flame Root Dynamics and Their Role in the Stabilisation of Lifted Flames, A. K. Gupta, A. De, S. K. Aggarwal, A. Kushari, A. K. Runchal (Eds.), *Advances in Energy and Combustion: Safety and Sustainability, Green Energy and Technology*, Springer Nature Singapore, Singapore, 2022, pp. 241–271.
- [53] A. M. Steinberg, I. Boxx, M. Stöhr, C. D. Carter, W. Meier, Flow–flame interactions causing acoustically coupled heat release fluctuations in a thermo-

- acoustically unstable gas turbine model combustor, *Combust. Flame* 157 (2010) 2250–2266.
- [54] I. Boxx, M. Stöhr, C. Carter, W. Meier, Temporally resolved planar measurements of transient phenomena in a partially pre-mixed swirl flame in a gas turbine model combustor, *Combust. Flame* 157 (2010) 1510–1525.
- [55] A. M. Steinberg, I. Boxx, M. Stöhr, W. Meier, C. D. Carter, Effects of Flow Structure Dynamics on Thermoacoustic Instabilities in Swirl-Stabilized Combustion, *AIAA J.* 50 (2012) 952–967.
- [56] N. Peters, *Turbulent Combustion*, Cambridge University Press, Cambridge, UK, 2000.
- [57] K. Radhakrishnan, J. B. Heywood, R. J. Tabaczynski, Premixed Turbulent Flame Blowoff Velocity Correlation Based on Coherent Structures in Turbulent Flows, *Combust. Flame* 42 (1981) 19–33.
- [58] R. Ciardiello, A. W. Skiba, R. L. Gordon, E. Mastorakos, Experimental assessment of the lean blow-off in a fully premixed annular combustor, *Exp. Therm. Fluid Sci.* 112 (2020) 109994.
- [59] G. T. Kalghatgi, Lift-off Heights and Visible Lengths of Vertical Turbulent Jet Diffusion Flames in Still Air, *Combust. Sci. Technol.* 41 (1984) 17–29.
- [60] W. J. A. Dahm, A. G. Mayman, Blowout limits of turbulent jet diffusion flames for arbitrary source conditions, *AIAA J.* 28 (1990) 1157–1162.
- [61] D. Feikema, R.-H. Chen, J. F. Driscoll, Enhancement of flame blowout limits by the use of swirl, *Combust. Flame* 80 (1990) 183–195.

- [62] J. F. Driscoll, Future Directions and Applications of Lean Premixed Combustion, N. Swaminathan, K. N. C. Bray (Eds.), *Turbulent Premixed Flames*, Cambridge University Press, Cambridge, UK, 2011, pp. 378–396.
- [63] A. K. Gupta, D. G. Lilley, N. Syred, *Swirl Flows*, Abacus Press, Royal Tunbridge Wells, UK, 1984.
- [64] N. Syred, J. M. Beér, Combustion in Swirling Flows: A Review, *Combust. Flame* 23 (1974) 143–201.
- [65] P. M. Anacleto, E. C. Fernandes, M. V. Heitor, S. I. Shtork, Swirl flow structure and flame characteristics in a model lean premixed combustor, *Combust. Sci. Technol.* 175 (2003) 1369–1388.
- [66] P. Fokaides, M. Weiß, M. Kern, N. Zarzalis, Experimental and Numerical Investigation of Swirl Induced Self-Excited Instabilities at the Vicinity of an Airblast Nozzle, *Flow Turbul. Combust.* 83 (2009) 511–533.
- [67] N. A. Chigier, J. M. Beér, Velocity and Static-Pressure Distributions in Swirling Air Jets Issuing From Annular and Divergent Nozzles, *J. Basic Eng.* 86 (1964) 788–796.